Astronomy & Astrophysics

XMM-Newton observations of the supernova remnant RX J1713.7–3946 and its central source

G. Cassam-Chenaï[1], A. Decourchelle[1], J. Ballet[1], J.-L. Sauvageot[1], G. Dubner[2], and E. Giacani[2]

[1] Service d'Astrophysique, CEA Saclay, 91191 Gif-sur-Yvette Cedex, France
e-mail: gcc@discovery.saclay.cea.fr

[2] Instituto de Astronomía y Física del Espacio, CC 67, Suc. 28, 1428 Buenos Aires, Argentina

Abstract. We present new results from the observations of the supernova remnant (SNR) RX J1713.7–3946 (also G347.3–0.5) performed in five distinct pointings with the EPIC instrument on board the satellite *XMM-Newton*. RX J1713.7–3946 is a shell-type SNR dominated by synchrotron radiation in the X-rays. Its emission (emission measure and photon index) as well as the absorption along the line-of-sight has been characterized over the entire SNR. The X-ray mapping of the absorbing column density has revealed strong well-constrained variations (0.4×10^{22} cm^{-2} $\leq N_H \leq 1.1 \times 10^{22}$ cm^{-2}) and, particularly, a strong absorption in the southwest. Moreover, there are several clues indicating that the shock front of RX J1713.7–3946 is impacting the clouds responsible for the absorption as revealed for instance by the positive correlation between X-ray absorption and X-ray brightness along the western rims. The CO and H I observations show that the inferred cumulative absorbing column densities are in excellent agreement with the X-ray findings in different parts of the remnant on condition that the SNR lies at a distance of 1.3 ± 0.4 kpc, probably in the Sagittarius galactic arm, instead of the commonly-accepted value of 6 kpc. An excess in the CO emission is found in the southwest suggesting that the absorption is due to molecular clouds. A search for OH masers in the southwestern region has been unsuccessful, possibly due to the low density of the clouds. The X-ray mapping of the photon index has also revealed strong variations ($1.8 \leq \Gamma \leq 2.6$). The spectrum is steep in the faint central regions and flat at the presumed shock locations, particularly in the southeast. Nevertheless, the regions where the shock impacts molecular clouds have a steeper spectrum than those where the shock propagates into a low density medium. The search for the thermal emission in RX J1713.7–3946 has been unsuccessful leading to a number density upper limit of 2×10^{-2} cm^{-3} in the ambient medium. This low density corresponds to a reasonable kinetic energy of the explosion provided that the remnant is less than a few thousand years old. A scenario based on a modified ambient medium due to the effect of a progenitor stellar wind is proposed and leads to an estimate of RX J1713.7–3946's progenitor mass between 12 and 16 $M_\odot$. The X-ray bright central point source 1WGA J1713.4–3949 detected at the center of SNR RX J1713.7–3946 shows spectral properties very similar to those of the Compact Central Objects found in SNRs and consistent in terms of absorption with that of the central diffuse X-ray emission arising from the SNR. It is highly probable that the point source 1WGA J1713.4–3949 is the compact relic of RX J1713.7–3946's supernova progenitor.

Key words. acceleration of particles – radiation mechanisms: non-thermal – ISM: supernova remnants – ISM: individual objects: G347.3-0.5 (RX J1713.7-3946) – X-rays: ISM – stars: individual: 1WGA J1713.4–3949

1. Introduction

Supernova remnants (SNRs) are well known to be sources of radio synchrotron emission from GeV relativistic electrons. During the last 10 years, X-ray synchrotron emission from TeV relativistic electrons has been discovered in several shell-type SNRs among which are SN 1006 (Koyama et al. 1995), RX J1713.7–3946 (Koyama et al. 1997; Slane et al. 1999) and RX J0852.0–4622 (Slane et al. 2001). This discovery bolstered the idea that collisionless shocks in SNRs are very powerful and efficient electron accelerators, possibly up to the "knee" of the cosmic-ray (CR) spectrum up to 10^3 TeV. It is reasonable to assume that protons are as well accelerated by these shocks.

RX J1713.7–3946 is a shell-type SNR located in the Galactic plane that was discovered with the *ROSAT* all-sky survey in the constellation Scorpius (Pfeffermann & Aschenbach 1996). It has a slightly elliptical shape with a maximum extent of 70′. The observation of the northwestern shell of the SNR with the *ASCA* satellite has shown the emission was exclusively non-thermal (Koyama et al. 1997).

Further observations with *ASCA* of most of the remnant did not reveal traces of the thermal emission, being likely overwhelmed by the bright X-ray synchrotron emission (Slane et al. 1999, hereafter SL99). An upper limit on the mean density of the ambient medium has been derived: $n_0 < 0.28 \, D_6^{-1/2}$ cm^{-3}, where D_6 is the distance in units of 6 kpc. Recently, this thermal component may have been detected in the interior of the

SNR over large fields-of-view using *ROSAT*, *ASCA* and *RXTE* satellites (Pannuti et al. 2003). However, some possible local variations of absorbing column density and photon index can compromise this interpretation.

An intriguing X-ray point-source (1WGA J1713.4–3949) with no optical and radio counterparts was also detected at the center of the remnant, being possibly a neutron star or an extra-galactic object (SL99). Recently, a combined *Chandra* and *XMM-Newton* spectral analysis of this source has shown that its X-ray properties (two-component spectrum, luminosity, absence of pulsations) resemble those of other compact central objects in SNRs and suggests that 1WGA J1713.4–3949 is the neutron star associated with RX J1713.7–3946 (Lazendic et al. 2003).

Neither the distance nor the age of RX J1713.7–3946 is well established. From the X-ray measurements of the column density toward this source, Koyama et al. (1997) derived a distance of 1 kpc, while SL99 proposed a larger distance of 6 kpc based on its probable association with three dense and massive molecular clouds and the HII region G347.6+0.2 located northwest to it. If the Sedov evolution is assumed with 6 kpc, an age of a few 10^4 years results, whereas an age of one order of magnitude below is compatible with 1 kpc. Hence, this nearer distance could be in agreement with the hypothesis proposed by Wang et al. (1997), based on historical records, that RX J1713.7–3946 is the remnant of the supernova (SN) that exploded in AD 393. The following studies adopted the largest distance of 6 kpc, until new *XMM-Newton* observations (Cassam-Chenaï et al. 2004b) that re-opened the whole distance question together with new high-resolution CO mm-wave observations (Fukui et al. 2003). These new results suggest possible indications of interaction between the SNR shock front and molecular gas located at 1 kpc on the northwest and southwest sides of the SNR.

In the radio, the emission arises from faint filaments aligned with the X-ray shell of RX J1713.7–3946, except for the brightest filament located in the northwestern rim which is perpendicular to the shock and coincident with part of the HII region G347.6+0.2 (SL99, Ellison et al. 2001; Lazendic et al. 2004).

GeV γ-ray emission was detected by the *EGRET* instrument to the northeast of the SNR (Hartman et al. 1999). This emission was interpreted as the decay of neutral pions attributed to the interaction of CR nuclei (accelerated at the shock in RX J1713.7–3946) with the massive and dense cloud assumed to be interacting with the remnant (Butt et al. 2001). By discussing the photon spectral index of the GeV source ($\alpha = 2.3 \pm 0.2$ which is expected from the hadronic interactions of CR source) and the non-detection in radio of the massive cloud. Butt et al. (2001) ruled out the possibility that electrons are responsible for the GeV luminosity.

At TeV γ-rays, the *CANGAROO* imaging Cerenkov telescope detected emission in the northwest of the SNR, which was interpreted as Inverse Compton (IC) emission from accelerated electrons (Muraishi et al. 2000). The low matter densities in the ambient medium is unfavorable for the interpretation in terms of π^0 decay process. A second *CANGAROO* observation of RX J1713.7–3946 leads to a TeV γ-ray spectrum (between 400 GeV and 8 TeV) whose photon spectral index

($\alpha = 2.8 \pm 0.2$) was shown to be consistent with the π^0 decay process and no other mechanism (Enomoto et al. 2002). However, such a spectrum would exceed the *EGRET* observed emission by a factor three (Reimer & Pohl 2002; Butt et al. 2002).

Several self-consistent models have been constructed using the broad-band spectrum from radio to γ-ray wavelengths, essentially for the northwest region of RX J1713.7–3946. Using a non-linear diffusive shock acceleration model, Ellison et al. (2001) were able to reproduce the broadband spectrum with synchrotron emission from shock-accelerated electrons in X-rays and IC emission in γ-rays. In this model, more than 25% of the shock kinetic energy goes into relativistic ions. Other attempts to reproduce the broadband spectrum were undertaken (Uchiyama et al. 2003; Pannuti et al. 2003; Lazendic et al. 2004).

In this paper, we provide for the first time a detailed description of the X-ray emission of RX J1713.7–3946 based on *XMM-Newton* observatory data. Thanks to the large field-of-view provided by the EPIC imaging spectrometers, we can cover the bulk of the SNR extent in a few pointings. The high sensitivity of *XMM-Newton* allows us to carry out a spectral analysis at medium-scale of the emission structures and then to produce for the first time a mapping of the spectral parameters of RX J1713.7–3946.

In Sect. 2, we present our observations and the different data reduction methods that we have used. In Sect. 3, we present the results obtained from the *XMM-Newton* data analysis. Section 4 contains a discussion on the potential association between the central point-like source 1WGA J1713.4–3949 and SNR RX J1713.7–3946 (Sect. 4.1), on the interaction between the remnant and clouds as well as on the SNR distance (Sect. 4.2), on the SNR age and energetics (Sect. 4.4) and finally on the overall picture that comes out from the results (Sect. 4.5). In Sect. 5, we summarize our results.

2. Data processing

2.1. Observation

SNR RX J1713.7–3946 was observed with the three EPIC instruments (namely the MOS1, MOS2 and pn cameras) on board the *XMM-Newton* satellite in the course of the AO-1 program. The observations were performed in five distinct pointings, each of around 10 ks duration. Table 1 indicates the date of observation and the OBS_ID for each pointing. The five pointings were chosen based on the *ROSAT* PSPC image (SL99) to allow a maximum coverage of the remnant and the possibility to extract a local X-ray background.

The pointings correspond schematically to the center, northeast, northwest, southwest and southeast (hereafter CE, NE, NW, SW, SE, respectively) parts of RX J1713.7–3946. During the observation, the MOS and pn cameras were operated in Full Frame and Extended Full Frame providing a temporal resolution of 2.6 s and 200 ms, respectively. For all the pointings, the medium filter was used to avoid contamination by visible sources contained in the field of view and to limit

Table 1. Duration after flare rejection. The location of the different pointings is shown in Fig. 2.

Pointing	Symbol	OBS_ID	Date	Exposure time (ks)			Comment
				MOS1	MOS2	pn	
NE	□	0093670101	2001-09-05	1.6	2.0	0	Very bad quality
NW	■	0093670201	2001-09-05	4.0	5.4	1.0	Bad quality
SW	●	0093670301	2001-09-08	15.3	15.5	10.0	Good quality
SE	○	0093670401	2002-03-14	12.2	12.2	6.8	Good quality
CE	△	0093670501	2001-03-02	13.0	13.2	7.3	Good quality

the number of low energy photons (and hence pile-up) coming from the bright X-ray point source 1WGA J1713.4–3949.

The potential neutron star 1WGA J1713.4–3949 is located roughly in the middle of the SNR at the position $\alpha_{J2000} = 17h13m28.4s$, $\delta_{J2000} = -39°49'54.5''$ (Lazendic et al. 2003). In the hope to detect thermal emission lines around 1 keV from 1WGA J1713.4–3949, the RGS data were also processed in the central pointing.

2.2. Flare rejection

The Science Analysis System (SAS version 5.3) was used for data reduction.

First, we generated calibrated events files with the SAS tasks *emchain* and *epchain*. To create light curves, spectra and images, we selected the single, double, triple and quadruple events (pattern ≤ 12) for the MOS cameras, and the singles and doubles (pattern ≤ 4) for the pn camera (with FLAG = 0 for all cameras). The data quality of the CE, SW, SE pointings is very good. However, it is not the case for the NE and NW pointings which are contaminated by soft protons flares. The method used to clean the data from the flares consists of applying a threshold on the light curves at high energy, i.e. where the EPIC cameras are almost insensitive to X-ray photons. We took a threshold of 18 counts per 100 s time interval in the 10–12 keV band for the MOS cameras (pattern ≤ 12) and a threshold of 22 counts per 100 s time intervals in the 12–14 keV band for the pn camera (pattern = 0). Table 1 indicates the remaining exposure time after flares cleaning for each EPIC camera.

2.3. Data reduction methods

In this section, we describe the different methods that have been used to create the images, the hardness ratio maps, the spectra and the mapping of the spectral parameters.

2.3.1. Images

All the mosaiced images of the X-ray emission presented here are background-subtracted, exposure and vignetting corrected (Sect. 3.1). The background used for the subtraction is only instrumental and is estimated by using a reference observation (Read & Ponman 2003) which was obtained with the same medium filter as in our observations. No correction for the local astrophysical background is made because we have no information on it in the center of the remnant and more further

it strongly varies around the remnant which renders difficult any extrapolation towards the interior. To correct for the exposure and the vignetting, we divide the mosaiced background-subtracted count image by its mosaiced exposure map which includes the vignetting correction using the SAS task *eexpmap*. Each time, the mosaiced count image is adaptively smoothed with the SAS task *asmooth* and the resulting template is applied to smooth both the mosaiced background-subtracted count image and its associated exposure map before the division.

We have not used the pn data for the intensity maps as it introduces some problems of homogeneity in the correction for vignetting and exposure due to the lack of pn data in the NE pointing (see Table 1).

2.3.2. Hardness ratio maps

To create hardness ratio maps, we divide two background-subtracted images made in different energy bands that are previously adaptively smoothed. For the smoothing, the template of the image with the lowest statistics is always applied to that with higher statistics. When we compute the ratio of the two maps, the statistical fluctuations can be amplified. To limit this effect, the MOS and pn data are used, but in return, the NE is missing in the hardness ratio maps (Sect. 3.3).

2.3.3. Spectra

All spectral analyses use the weight method described in Arnaud et al. (2001) to correct for the vignetting. For the background subtraction, we always use the double subtraction method described in Arnaud et al. (2002) except for the mapping of the spectral parameters (see below, Sect. 2.3.4). This method allows us to take into account the difference, at low energy, between the local astrophysical background of our observations and the one found in the reference observation. This is done for local spectral analyses which require a precise knowledge of the spectrum at low energy (Sect. 3.3). In our observations, there are two regions where the local astrophysical background can be extracted with enough statistics: the SW and the SE. Each time, we choose the nearest available local astrophysical background for each selected region.

The spectra are grouped so that each bin has a signal-to-noise ratio greater than 5σ. To fit the spectra, we use XSPEC (version 11.2, Arnaud 1996). The chosen on-axis response files are `m*_medv9q20t5r6_all_15.rsp` for MOS and `epn_ef20_sdY9_medium.rsp` for pn.

2.3.4. Mapping of the spectral parameters

The X-ray spectrum of SNR RX J1713.7–3946 can be well fitted by a simple absorbed power-law model the spectral parameters of which are the absorbing column N_H and the photon index Γ. Here, we describe how we map the spatial variations of these two parameters (Fig. 4).

First, we build a spatial grid which takes into account the statistics so that we have approximately the same number of counts in each grid pixel. The spatial grid is constructed from a mosaiced count image (MOS+pn) between 0.8–10 keV where all the point-like sources have been removed. The mean number of total counts in a pixel is fixed to 9000 counts from this image which corresponds approximately to 2500 and 4000 counts in most of the boxes of the MOS and pn cameras, respectively.

For each pixel of the grid, we extract the X-ray spectra (MOS, pn) and fit them with a simple absorbed power law. A map of these parameters (N_H, Γ) is constructed from the best-fit values in each grid pixel.

In this spectral analysis, we use a single background-subtracted method (as described for the images, Sect. 2.3.1) since it is not possible to have the true local astrophysical background in each grid pixel. Because of that, the spectral bins only above 0.8 keV are selected, *i.e.* where the reference background provided by Read & Ponman (2003) is almost one order of magnitude below the spectrum of our observations. We have checked that the absence of spectral bins below 0.8 keV did not change significantly the value of the spectral parameters in the X-ray bright regions.

There is no significant difference between the single and the double background-subtraction methods for the brightest regions. Nevertheless, in the X-ray faint regions, the effect of the double substraction is to increase N_H and Γ by a factor ~10–15% which is not enough to alter our results and interpretation.

3. X-ray results

Unlike the X-ray spectra of typical shell-like SNRs which exhibit emission lines, the spectrum of RX J1713.7–3946 is found to be featureless as shown for example in Fig. 1. This suggests a non-thermal origin and has been interpreted as synchrotron X-ray emission from TeV shock accelerated electrons (SL99). RX J1713.7–3946 is a second example, after SN 1006, of a shell-like SNR for which non-thermal emission dominates the X-ray flux, but more extreme in the sense that no thermal emission has been unambiguously detected yet. Unlike SN 1006, a symmetrical limb-brightened type Ia remnant located in a high-latitude environment, RX J1713.7–3946 has a quite distorted morphology which may be related to its complex surrounding environment in the Galactic plane and is likely to be the remnant of a type II explosion as suggested by the presence of a central point source detected at its center.

In Sect. 3.1, we describe in detail the unusual X-ray morphology of RX J1713.7–3946, and compare it to the radio continuum morphology. In Sect. 3.2, we trace and accurately diagnose the spectral variations of the synchrotron emission. In
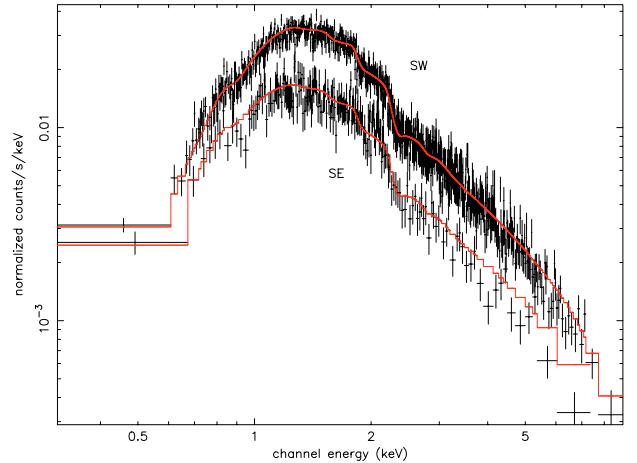

Fig. 1. EPIC pn spectra (double background subtraction) of the SW and SE regions of SNR RX J1713.7–3946. The fit with a power-law model gives $N_H = 0.71 \pm 0.02 \times 10^{22}$ cm^{-2} and $\Gamma = 2.33 \pm 0.03$ for the SW region and $N_H = 0.57 \pm 0.03 \times 10^{22}$ cm^{-2} and $\Gamma = 2.16 \pm 0.06$ for the SE region at a 90% confidence level.

Sect. 3.3, we search for the thermal emission and constraints on its properties. Finally, in Sect. 3.4, we intent to give better spectral constraints on the nature of the point-like source 1WGA J1713.4–3949 to provide arguments in favor or against a potential association with SNR RX J1713.7–3946.

3.1. X-ray morphology

The good spatial resolution and sensitivity of *XMM-Newton* combined with its large field-of-view allow us for the first time to both have an overall view of RX J1713.7–3946 and resolve some X-ray emission features not seen before in the *ROSAT* and *ASCA* images (SL99, Uchiyama et al. 2003). Figure 2 shows the 5 pointings mosaiced image of RX J1713.7–3946 in the 0.8–2 keV (left panel) and 2–10 keV (right panel) energy bands. However, the 5 pointings are not enough for a complete coverage of the SNR. The general shape of this distorted remnant resembles roughly an ellipse stretched out along the NW-SE axis over ~70′ corresponding to ~20 pc at 1 kpc or ~120 pc at 6 kpc. An overall view of RX J1713.7–3946 obtained with *ASCA* (Uchiyama et al. 2003) shows that the boundaries of the SNR are irregular and suggests that the remnant extends farther to the north.

Except for the point-like sources, the comparison between the low energy and high energy images (see Fig. 2) does not show significant changes in the X-ray morphology at first sight, at least for the brightest X-ray features. From these images, the X-ray emission can be schematically classified in three distinct levels. The lower intensity one is due to the diffuse X-ray emission of the local astrophysical background. In both images, it can be found (in blue-black) on the outside of the NE, NW, SW and SE pointings. It stands out that the local astrophysical background intensity varies around the remnant. This fact is expected since RX J1713.7–3946 lies just below the Galactic Ridge in an environment where the properties of the interstellar gas rapidly change with Galactic latitude (which is the direction
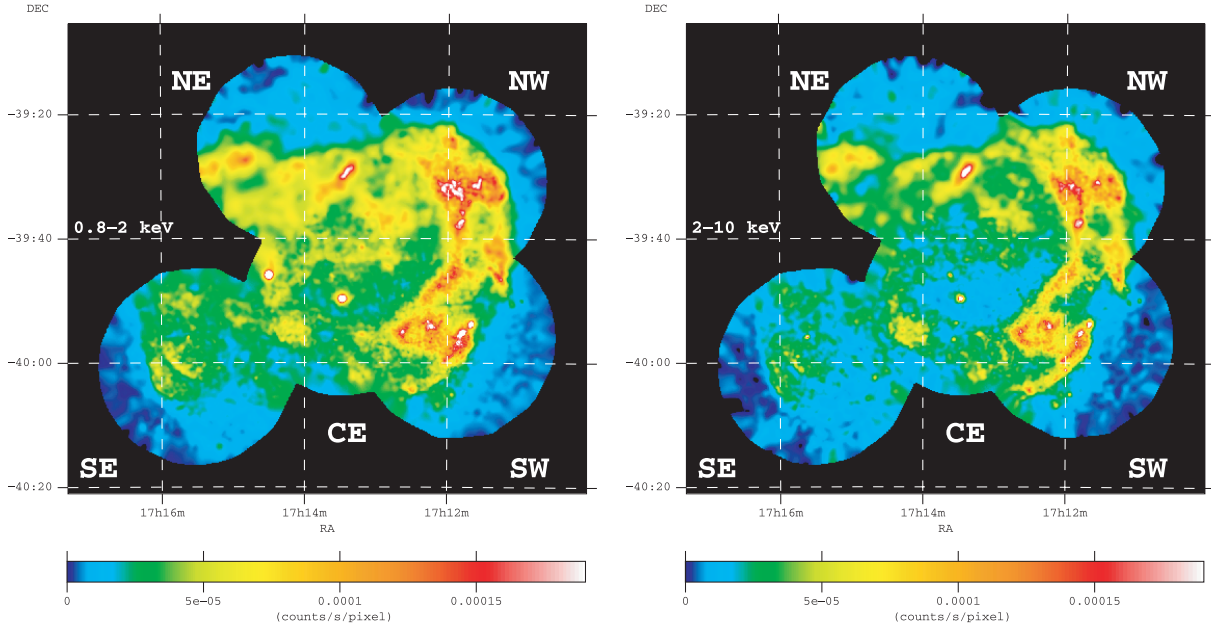
Fig. 2. *Left panel*: MOS mosaiced image of SNR RX J1713.7–3946 in the 0.8–2 keV energy band. *Right panel*: same as left panel but in the 2–10 keV energy band. The neutron star 1WGA J1713.4–3949 is located in the middle of the CE pointing. Both images were adaptively smoothed to a signal-to-noise ratio of 10. The scaling is square root with the higher cut fixed to 30% of the SNR maximum X-ray brightness. The color bar numbers are in units of counts/s/pixel with a pixel size of 4″. The bad resolution in the NE is due to a very short exposure time (see Table 1). Moreover, it is possible that the smoothing has removed a few small-scale features in this NE pointing.

where the SNR is more stretched out). The medium intensity level corresponds to the diffuse and faint X-ray emission arising from the SNR which clearly dominates in the 0.8–2 keV energy band (in green and also in blue). The higher intensity level is made of a more structured emission which appears in both images but more clearly at high energy in the 2–10 keV band (in yellow and red). Its surface brightness is about twice that of the diffuse emission associated with the SNR.

Both the NW and SW limbs are very bright in X-rays. The X-ray emission in the western half is more structured than anywhere else in the SNR. At large scales, a double-ring morphology stands out. The internal ring is more or less circular whereas the external one looks broken into a few arcs. At smaller scales, the *Chandra* image of the NW region shows that the brightest X-ray features correspond to thin filaments of 20″ apparent width or hot spots embedded in a diffuse plateau emission (Uchiyama et al. 2003; Lazendic et al. 2004). This is confirmed by *XMM-Newton* in the NW and also in the SW.

In spite of its bad quality, the NE observation shows that the inner circular thin shell seen in the west seems to continue there (see Fig. 2, right panel). Nevertheless, the diffuse X-ray emission from the NE pointing seems to exhibit a concave border between the remnant and the ambient medium (green emission in Fig. 2, left panel). Such a shape is not naturally expected from an explosion into a homogeneous low density interstellar medium. That shape must be caused by some obstacles either interacting with the SNR or obstructing the X-ray emission arising from it.

The X-ray emission from the SE is weak and diffuse but even so we distinguish a possible border between the SNR and the ambient medium.

Finally, the central part of the SNR shows diffuse X-ray emission rather weaker than in the NW and SW but similar to what is observed in the SE. In addition, two point sources are observed. The first one is 1 WGA J1714.4-3945 located at the position $\alpha_{J2000} = 17h14m30s$, $\delta_{J2000} = -39°46'00''$ which disappears above 2 keV. The second one located in the middle of the CE pointing is 1WGA J1713.4–3949, a potential neutron star, which will be studied in detail in Sect. 3.4.

Figure 3 shows a high-resolution radio image obtained at 1.4 GHz with *ATCA* (from Lazendic et al. 2004) overlaid with the X-ray contours. The radio morphology of RX J1713.7–3946 is quite complex, with the brightest emission corresponding to the HII region G347.6+0.2, to the NW corner. A well defined ring of emission, about 15′ in size, is visible in the interior of the SNR. This radio feature matches the inner X-ray bright ring, particularly towards the northern, northwestern and western sides. Also, a very good correspondence is observed on the X-ray-bright outer rim to the SW. The observed similar morphology in the radio and in the X-rays strongly suggests that the synchrotron emission detected at the two spectral domains must originate in the same electron population accelerated at the shocks.

3.2. Spatial and spectral characterization of the synchrotron emission

In this section, we present the maps of absorbing column density and photon index (method described in Sect. 2.3.4).

Figure 4 (left panel) shows the mapping of absorbing column density in the line-of-sight at medium scale. The mean relative error on the absorbing column in each pixel grid
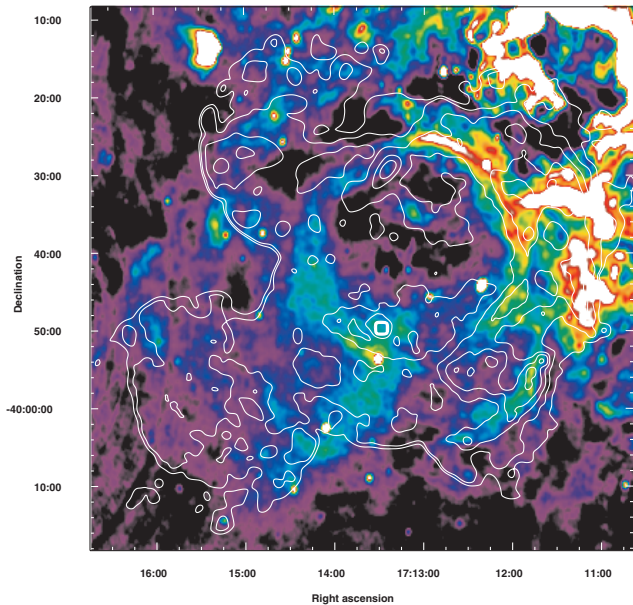
Fig. 3. 1.4 GHz *ATCA* radio image (courtesy of J.S. Lazendic) overlaid with the 2–10 keV contour of SNR RX J1713.7–3946. The scaling is linear. The contour values start at 10^{-5} MOS counts/s/pixel and are square root spaced up to 1.9×10^{-3} counts/s/pixel with a pixel size of $4''$.

is ~9% with a maximum value of 16%. The variations of absorbing column density are strong with $N_{\rm H}$ varying from ~0.4×10^{22} cm^{-2} to ~1.1×10^{22} cm^{-2}. In the SE and CE pointings, $N_{\rm H}$ is low with a value ~$0.4-0.5 \times 10^{22}$ cm^{-2} whereas it is larger in the NW ($N_{\rm H} \sim 0.6-0.7 \times 10^{22}$ cm^{-2}) and even more in the SW ($N_{\rm H} \sim 0.8-1.1 \times 10^{22}$ cm^{-2}). Figure 5 (top panel) illustrates the variations of absorbing column from two spectra extracted in the SW region.

The comparison between the mapping of absorbing column density and the X-ray brightness contours (Fig. 4, left panel) suggests that there is a positive correlation between them. Figure 6 shows the X-ray brightness at 1 keV versus $N_{\rm H}$ in each grid pixel. We see that the regions of large (small) $N_{\rm H}$ correspond to those of high (weak) X-ray brightness confirming the significance of the observed correlation. The fact that high absorbing column coincides with brighter X-ray emission, as observed to the SW (and NW), is unexpected. Indeed, a dense cloud located in front of an X-ray source and not related to it must diminish the photon source flux in our direction (at low energy in particular). That we observe a positive correlation between the absorbing column density and the X-ray brightness means that the increased ambient density somehow amplifies the X-ray brightness. This strongly suggests that the remnant is interacting in the brightest regions with part of the line-of-sight absorbing material.

Figure 4 (right panel) shows the mapping of the photon spectral index. The mean relative error on the photon index value in each grid pixel is ~4% with a maximum value of 7%. The variations of photon index are important given that Γ varies from ~1.8 to ~2.6. The spectrum is steep in the faint central region whereas it is a bit flatter in the NW and even more so in the SE. The fact that the spectrum gets steeper as we move

inwards away from the shock front is expected in SNRs. This effect is generally explained by the adiabatic expansion of the remnant and the synchrotron radiative losses (Reynolds 1998) as is also observed in SN 1006. In the SW, the spectrum is generally steep, but some regions exhibit strong variations of spectral index as is shown in Fig. 4 (right panel). For illustration, Fig. 5 (bottom panel) shows the spectrum of two regions in the SW, for which the index is very different.

The synchrotron X-ray morphology, though quite complex, can be related to the absorption along the line-of-sight (or equivalently brightness). On the one hand, there is a weakly absorbed SE region which seems to extend far away from the center of the SNR (taken as the point-like source 1WGA J1713.4–3949), and on the other hand, a strongly absorbed western region which is closer and where RX J1713.7–3946 is suspected to interact with the material that causes the absorption. Such an asymmetry in the morphology and the absorption must be the result of different ambient densities around the remnant. To investigate how particle acceleration is modified in different environments, we have selected two sets of points located at the presumed shock locations: the one in the SW external rim coincident with the radio emission (see Fig. 3) and in the SE. These points are shown in Fig. 7 in the absorbing column density-X-ray brightness plane (top panel) and in the photon index-X-ray brightness plane (bottom panel). It is obvious that two groups stand out. The regions where the shock propagates in the SW have a steep spectrum ($\Gamma \sim 2.3-2.7$) and those where the shock propagates in the SE have a flat spectrum ($\Gamma \sim 1.9-2.2$)[1]. This point is discussed further in Sect. 4.3.

3.3. Thermal emission

Determining the thermal properties of the hot gas is crucial to constrain the evolutionary state of the remnant. That the thermal emission is not clearly detected in SNR RX J1713.7–3946 however sets strong limits on the temperature of the hot gas and, above all, on its mean density. On the one hand, the temperature determination is important because it gives an idea of the shock velocity (with a few assumptions on the heating of the electrons behind the shock). On the other hand, the estimation of the mean ambient medium density is crucial to provide an estimate of the swept-up mass (assuming that the distance to the SNR is known) which then constrains the phase of evolution of the remnant.

To characterize the synchrotron emission (Sect. 3.2), the spectra of SNR RX J1713.7–3946 were modelled by an absorbed phenomenological power-law which provides, at the first order, an excellent representation of the data. To search for the thermal emission, we add a second component, the thermal model, which will not necessarily improve the spectral fit but will be essential to constrain the properties of the thermal gas. For this task, it is important to look at spectrally homogeneous areas since the spectrum of a region with strong variations of $N_{\rm H}$ and Γ modelled with an uniformly absorbed

---

[1] The effect of the double subtraction method (cf. Sect. 2.3.4) is to tighten the spectral index values between the SW and the SE. However the two distinct groups remain.
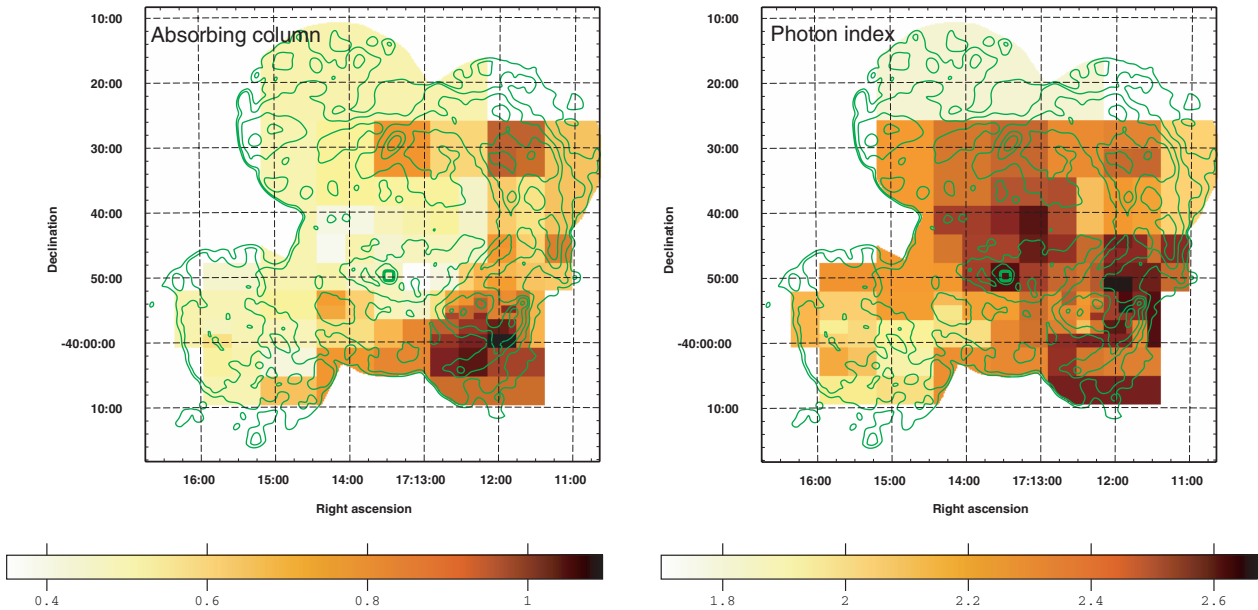
Fig. 4. *Left panel*: absorbing column map N_H (in units of 10^{22} cm^{-2}) overlaid with the contour of the 2–10 keV image of SNR RX J1713.7–3946. The contour values start at 10^{-5} MOS counts/s/pixel and are square root spaced up to 1.9×10^{-3} counts/s/pixel with a pixel size of 4″. The big boxes of our adaptive grid found in the NE and NW pointings are due to the low exposure time there. *Right panel*: photon index map overlaid with the same X-ray contours. In both images, the scaling is linear.

single power-law could simulate artificially the need for a thermal additional component instead of a second non-thermal component. Eight particular regions (point-like sources removed) with no or few spectral variations were chosen based on the low-energy and high-energy hardness ratio maps, and such that they have enough statistics. They are shown in Fig. 8. Although the hardness ratio maps do not give the value of Γ or N_H, they permit us to retain more precise spatial information than in the photon index or absorbing column map which intrinsically depend on the shape and size of the pixels of the grid.

Like in previous studies where an attempt to investigate the thermal emission properties was done (SL99, Pannuti et al. 2003), we will first assume the plasma to be in an equilibrium ionization state. This hypothesis will be discussed further. In the following study, the elemental abundances are fixed to solar.

First, we investigate how our previous results (Sect. 3.2) might be modified by the addition of a thermal component in the model. Table 2 gives the best-fit parameters obtained for an absorbed power-law model in each of the eight regions selected for this analysis, while Table 3 gives the results obtained with the addition of a thermal equilibrium ionization component. It appears that the introduction of the thermal model improves very slightly the fit ($\Delta\chi^2 \sim 10-30$) and does not change qualitatively the results found for the non-thermal emission as is shown in Fig. 9. The derived parameters (N_H, Γ) are similarly changed for all the eight regions: they always get slightly larger as we add the thermal component to the model.

The comparison between the fluxes of the thermal emission obtained in different regions of the SNR gives an idea of the spatial distribution of the shocked medium density. Table 3

gives the value of $\int n_e n_H \, dl$ and the temperature found for the thermal emission (for the 8 regions). The range of temperatures kT_e is always below 1 keV. The values of the square density integrated along the line-of-sight are rather homogeneous ($\sim 1 \times 10^{16}$ cm^{-5}). We note however that this quantity seems to increase from the SNR shock front (regions 1 and 8) to the interior (regions 2 and 6) when we look at a temperature around 0.5–0.6 keV.

The postshock electronic number density $\hat{n}_e \equiv \left(\int n_e^2 \, dl / \int dl\right)^{1/2}$ is determined by (assuming that $n_e = 1.21 \, n_H$):

$$\hat{n}_e = 8.21 \times 10^{-2} \left(\frac{\int n_e n_H \, dl}{10^{16} \text{ cm}^{-5}}\right)^{1/2} \left(\frac{D}{1 \text{ kpc}}\right)^{-1/2}$$
$$\times \left(\frac{\theta_s}{1'}\right)^{-1/2} \left(1 - \left(\frac{\theta_r}{\theta_s}\right)^2\right)^{-1/4} \text{ cm}^{-3} \quad (1)$$

where the angular distance between the center of the SNR (taken as the position of the central point-like source 1WGA J1713.4–3949) and the considered region is θ_r while that of the blast-wave is θ_s. Table 4 shows that the average postshock electronic density is approximately at the same level over the SNR ($\hat{n}_e \sim 2.1^{+0.8}_{-0.9} \times 10^{-2}$ cm^{-3} for $D = 1$ kpc), being a bit larger in the interior ($\hat{n}_e \sim 2.4 \pm 0.5 \times 10^{-2}$ cm^{-3}) than close to the shock ($\hat{n}_e \sim 1.9 \pm 0.5 \times 10^{-2}$ cm^{-3}). In a Sedov model, the average postshock density is similar to the mean number density in the ambient medium in the inner regions of the SNR. Then, the postshock densities lead to a mean hydrogen number density n_0 of the ambient preshock medium between 0.010 and 0.024 $D_1^{-1/2}$ cm^{-3}.

Nevertheless, because of the extremely low density in the ambient medium, the assumption of equilibrium ionization state does not hold any more. Indeed, since the
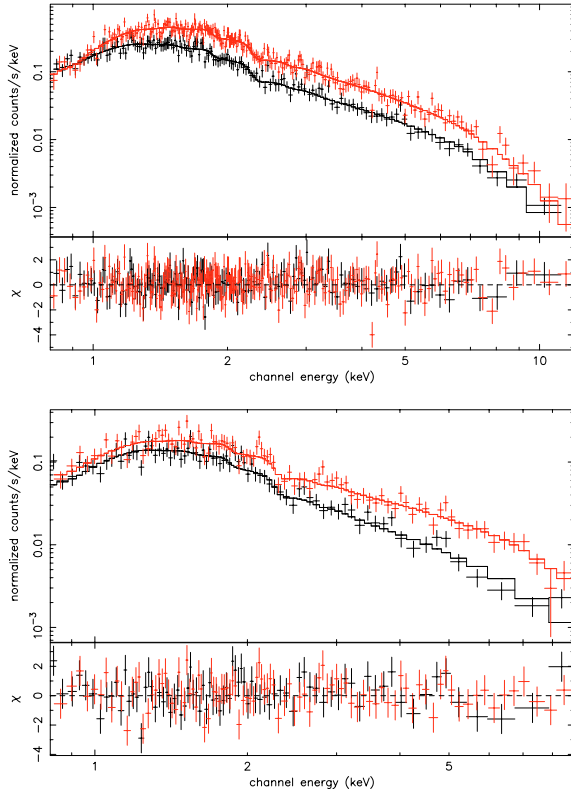
Fig. 5. *Top panel*: pn spectra of two SW regions of similar brightness ($\sim 2.8 \times 10^{-4}$ photons/cm²/s/keV/arcmin²) and same photon index ($\Gamma \sim 2.4$) but with different absorbing column densities. The absorbing column is $1.09 \pm 0.05 \times 10^{22}$ cm⁻² for the top spectrum (17h11m58.2s, –39°59′44.5″) and $0.77 \pm 0.05 \times 10^{22}$ cm⁻² for the other one (17h11m52.5s, –39°55′54.6.″). *Bottom panel*: pn spectra of two SW regions of similar brightness ($\sim 2 \times 10^{-4}$ photons/cm²/s/keV/arcmin²) and same absorbing column ($N_H \sim 0.9 \times 10^{22}$ cm⁻²) but with different photon index. $\Gamma = 2.07 \pm 0.10$ for the top spectrum (17h12m26.7s, –39°57′34.4″) and $\Gamma = 2.66 \pm 0.12$ for the other one (17h11m52.6s, –39°54′49.0″).
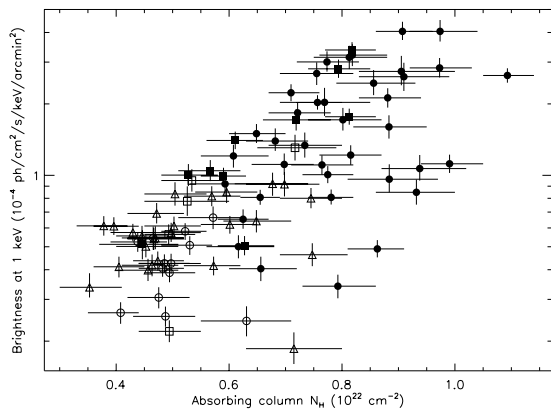
Fig. 6. Correlation plot between the absorbing column N_H (in units of 10^{22} cm⁻²) and the normalized brightness at 1 keV. Each point corresponds to the value found for a particular pixel of the mapping grid (Sect. 2.3.4) and the error bars are given at a 90% confidence level. The symbols are defined as follow (cf. Table 1): □ for NE, ■ for NW, ● for SW, ○ for SE, △ for CE. The regions which are the more absorbed are the brightest. They are mainly located in the SW. The regions which have small N_H are the less bright and are found in the CE and SE.
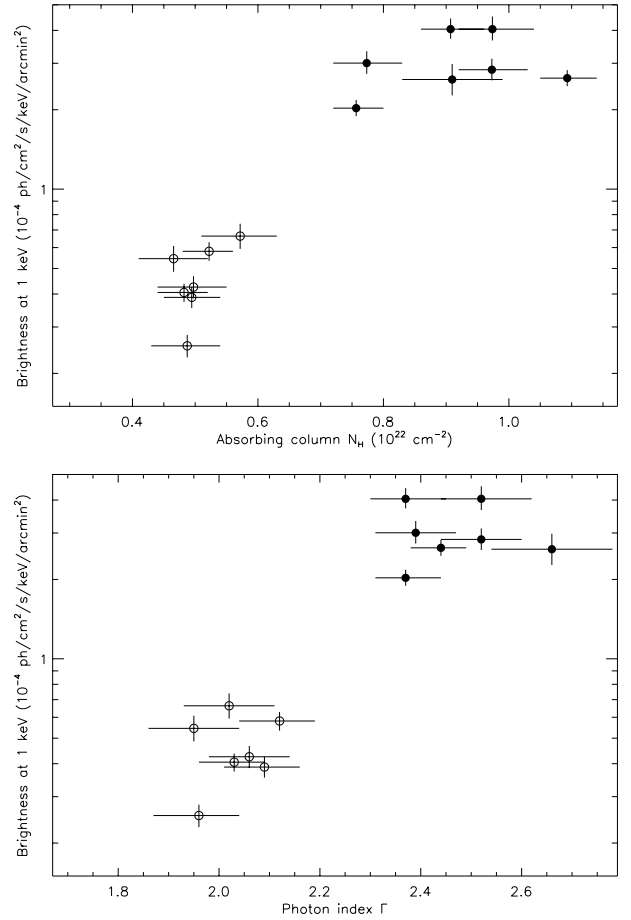
Fig. 7. *Top panel*: correlation plots at the shock location in the SW (●) and SE (○) regions between the absorbing column N_H (in units of 10^{22} cm⁻²) and the normalized brightness at 1 keV (in units of 10^{-4} photons/cm²/s/keV/arcmin²). Each point corresponds to the value found for a particular pixel of the mapping grid (Sect. 2.3.4) and the error bars are given at a 90% confidence level. The points of the SW region are selected so that they are above 2.0×10^{-4} photons/cm²/s/keV/arcmin². *Bottom panel*: correlation plots between the photon index Γ and the normalized brightness at 1 keV for the same set of points as above. The error bars are given at a 90% confidence level.

ionization age must be lower than $\max(\hat{n}_e)\, t_s = 9.0 \times 10^8 \left(\frac{D}{1\,\text{kpc}}\right)^{1/2} \left(\frac{t_s}{10^3\,\text{yr}}\right)$ s cm⁻³ where t_s is the SNR age, even a remnant of 10^5 years old would be insufficient to reach the ionization equilibrium. Consequently, we have applied a non-equilibrium model instead of the equilibrium model while keeping the power-law model. This has been done by relating the ionization age τ to the emission measure as described in Cassam-Chenaï et al. (2004a, Sect. 6.3). It is found that this model does not improve the fit obtained with the power-law model alone. In the power-law plus non-equilibrium model, the power-law characteristics are the same as those obtained for a single power-law model (Table 2). The temperature of the thermal gas is found to be around 3 keV but is poorly constrained. Moreover, an upper limit on the ionization age of 4.5×10^8 s cm⁻³ is obtained. Assuming $t_s = 1600$ years (cf. Sect. 4.4), this leads to an upper limit of

$2.6 \times 10^{-2} D_1^{-1/2}$ cm^{-3} for the average postshock electronic density and $0.02 D_1^{-1/2}$ cm^{-3} for the mean hydrogen number density of the ambient preshock medium (D_1 is the distance in units of 1 kpc).

Whatever the thermal model (equilibrium or non-equilibrium) added to the nonthermal model, we derive similar mean hydrogen number densities n_0 of the ambient preshock medium. In the following, we will adopt the upper limit $n_0 \leq 2 \times 10^{-2} \, D_1^{-1/2}$ cm^{-3}.

3.4. Central source 1WGA J1713.4–3949

The nature of the point-like source 1WGA J1713.4–3949 located at the center of SNR RX J1713.7–3946 is not clearly established: a neutron star or a background extra-galactic source seem to be possible interpretations (SL99). However, the neutron star hypothesis is the most attractive because of the lack of radio emission and as optical counterpart, and because the derived upper limit column density from the *ASCA* X-ray spectra is comparable to the total absorption through the Galaxy in this direction (SL99).

Recently, Lazendic et al. (2003) have shown that no pulsation and no long-term flux variability have been found using the *ASCA*, *RXTE*, *Chandra* and *XMM-Newton* data. Besides, the radio pulsar PSR J1713-3945 (α_{J2000} = 17h14m23.3s, δ_{J2000} = $-39°45'47.5''$, P = 392 ms, D = 4.3 kpc) is not associated with the X-ray point source 1WGA J1713.4–3949 nor with SNR RX J1713.7–3946.

Here, we intend to give better spectral constraints on the nature of this source 1WGA J1713.4–3949 thanks to the high sensitivity of *XMM-Newton*. The spectral analysis of the source, as well as the knowledge of the absorbing column density map of the remnant (Sect. 3.2), must provide arguments in favor of or against a potential association with the SNR RX J1713.7–3946.

We extracted the source counts from a $25''$ radius circle and the background was taken in an annulus of radii R_{min} = $60''$ and R_{max} = $200''$ around the point source center. The background subtracted source count rates obtained are 0.410 ± 0.006, 0.413 ± 0.006 and 1.148 ± 0.013 counts s^{-1} for MOS1, MOS2 and pn, respectively. We extracted the spectrum of the central source in the 0.3–12.0 keV band. As shown in Fig. 10, it does not extend higher than 6.5 keV. No thermal spectral emission lines are found in the EPIC data, nor in the RGS data around 1 keV.

We first considered one component simple models, the results of which are summarized in Table 5. Fitting the spectrum with a simple absorbed power law yields a large photon index Γ = 4.24 ± 0.06. Such a value is much steeper than what is generally found in other young neutron stars which are well known for their non-thermal emission from relativistic particles accelerated in the pulsar magnetosphere (for instance, Willingale et al. 2001 give Γ = 1.63 ± 0.09 for the Crab pulsar). Moreover, the fit overestimates the spectrum at high energy resulting in a bad χ_r^2 = 1.58 (for 475 d.o.f.). The column density N_H = $1.10 \pm 0.03 \times 10^{22}$ cm^{-2} inferred exceeds the values found in the SNR surrounding medium.

If the source is not an active pulsar but a neutron star, thermal radiation from the star surface can be observed. A single blackbody model improves the fit (χ_r^2 = 1.31 for 475 d.o.f.) but does not reproduce the hard emission. It yields a high temperature of kT = 0.40 ± 0.2 keV, a small radius R = $0.37 \pm 0.01 \, D_1$ km of emitting area and a luminosity of $L = 0.49 \pm 0.02 \times 10^{33} \, D_1^2$ erg s^{-1} where D_1 is the distance in units of 1 kpc. The value of L is lower than predicted by standard cooling neutron star models for which the typical luminosity is $\sim 10^{34}$ erg s^{-1} for a neutron star of a few thousand years (e.g. Tsurata 1998). Such a low luminosity could be explained by an accelerated cooling process. However the small size of emitting area along with the high temperature means that the cooling cannot take place from the entire neutron star surface. Note that the temperature, radius and luminosity of the central point source 1WGA J1713.4–3949 are almost identical to what is found for the central point source in SNR RX J0852.0-4622 (also G266.2-1.2 or "Vela Junior") adopting a distance of 1 kpc (see Becker & Aschenbach 2002; Kargaltsev et al. 2002). The column density N_H = $0.35 \pm 0.02 \times 10^{22}$ cm^{-2} is lower than the values found in the SNR. We note that our range of temperatures is in the error bars given by SL99 whereas both our column density and radius are lower (in SL99, N_H = $0.52^{+0.18}_{-0.16} \times 10^{22}$ cm^{-2} and R = $0.50^{+0.17}_{-0.11} \, D_1$ km). The latter point should be related to the weak flux reduction. Indeed, the unabsorbed flux in the 0.5–5.0 keV energy band obtained with *ASCA* (5.3×10^{-12} erg cm^{-2} s^{-1}, SL99) is larger than the one obtained with *XMM-Newton* (3.8×10^{-12} erg cm^{-2} s^{-1}).

A simple thermal bremsstrahlung yields an excellent fit (χ_r^2 = 1.05 for 475 d.o.f.) with a high temperature kT = 0.94 ± 0.2 keV and an absorbing column density of N_H = $0.70 \pm 0.02 \times 10^{22}$ cm^{-2} compatible with the value derived at the center of the SNR.

A more precise description of 1WGA J1713.4–3949 can be given by testing more elaborate models with two spectral components. Table 6 summarizes the results obtained. To allow for different emission mechanisms, we first introduce a soft thermal component arising from the neutron star surface with a blackbody model and a non-thermal component described by a power law due to relativistic particles heating the polar caps of the neutron star. The resulting fit is similar to that obtained with the thermal bremsstrahlung model. The photon index Γ = 4.24 ± 0.06 is steep in comparison to the spectral index found in young neutron stars. Both the luminosity and the temperature are a bit lower than what is expected for a cooling neutron star of a few thousand years (Tsurata 1998). The column density N_H = $0.91 \pm 0.05 \times 10^{22}$ cm^{-2} inferred exceeds the values found in the SNR center.

A two-component blackbody model allows us to represent the non-uniformity of the surface temperature distribution of the neutron star. The double blackbody is found to describe the data best (χ_r^2 = 1.04 for 473 d.o.f.) resulting in temperatures of kT_1 = $0.57^{+0.07}_{-0.05}$ keV and kT_2 = $0.32^{+0.02}_{-0.03}$ keV with R_1 = $0.59^{+0.10}_{-0.09} \, D_1$ km and R_2 = $0.32^{+0.02}_{-0.03} \, D_1$ km for the radii of the emitting areas. It suggests that the first thermal component is emitted from a small fraction of the neutron star surface since the expected radius of a neutron star is $\sim 10-15$ km. The second thermal component emission can be due to the heating
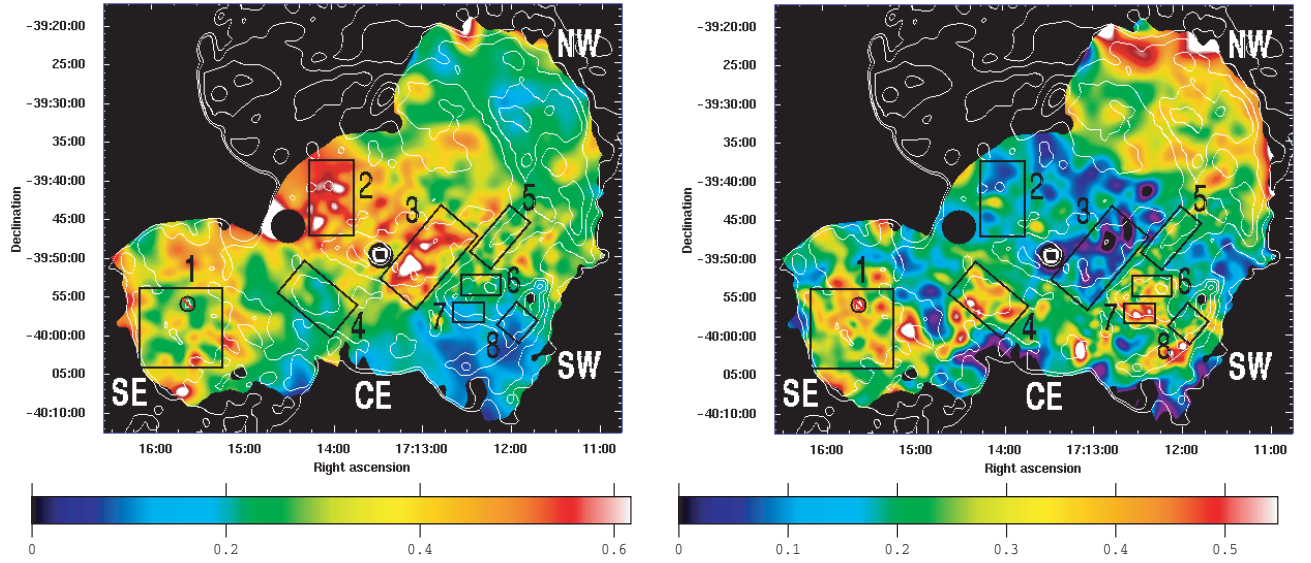
Fig. 8. *Left panel*: spatial distribution of the hardness ratio [0.7–0.9 keV]/[1.0–1.3 keV] overlaid with the contour of the 2–10 keV image of SNR RX J1713.7–3946. *Right panel*: spatial distribution of the hardness ratio [5–8 keV]/[1.6–2.0 keV] overlaid with the same X-ray contours. In both images, the point-like sources have been removed. The scaling is linear. Regions of extraction used for the search of the thermal emission are shown and labeled from 1 to 8.

Table 2. Best fit parameters for the power-law model using the MOS and pn data all at once. The errors are in the range $\Delta\chi^2 < 2.7$ (90% confidence level) on one parameter. The regions shown in Fig. 8. *Norm* is given in units of photons/cm^2/s/keV/arcmin^2 at 1 keV.

Region	χ^2 (d.o.f.)	N_H (10^{22} cm^{-2})	Γ	*Norm*
1	952 (909)	0.66 (0.64–0.69)	2.34 (2.29–2.39)	6.06e−5 (5.75–6.41)
2	530 (468)	0.54 (0.51–0.56)	2.68 (2.61–2.75)	6.94e−5 (6.51–7.39)
3	533 (495)	0.47 (0.45–0.49)	2.58 (2.51–2.65)	3.59e−5 (3.36–3.86)
4	540 (518)	0.77 (0.74–0.82)	2.23 (2.17–2.29)	8.33e−5 (7.73–8.93)
5	656 (632)	0.68 (0.66–0.70)	2.46 (2.42–2.51)	1.65−e4 (1.58–1.73)
6	738 (642)	0.77 (0.75–0.80)	2.30 (2.26–2.35)	2.26e−4 (2.15–2.38)
7	394 (356)	0.89 (0.85–0.94)	2.15 (2.09–2.22)	1.54e−4 (1.42–1.67)
8	822 (761)	1.05 (1.02–1.08)	2.52 (2.48–2.56)	3.04e−4 (2.90–3.20)

of polar caps by relativistic particles which are accelerated in the magnetosphere or to anisotropic heat conductivity in the neutron star crust (e.g. Becker & Aschenbach 2002). The fit yields a column density $N_H = 0.47 \pm 0.03 \times 10^{22}$ cm^{-2} that is compatible with the values found in the central part of the remnant.

These results are globally compatible with those of Lazendic et al. (2003).

4. Discussion

4.1. On the nature of the central source

To say whether the neutron star is associated with SNR RX J1713.7–3946 or not, we must compare the results of our spectral analysis with the values found for other types of compact objects found in other SNRs. On the other hand, the absorbing column value derived from the best-fit model must be consistent with the absorbing column density found for the diffuse emission of the remnant in the central region.

The spectral properties (cf. Table 6) of the central point source 1WGA J1713.4–3949 are very similar to those of the Compact Central Objects (CCOs) in "Vela Junior" (SNR G266.1-1.2 or RX J0852-4622), in Cas A and in Puppis A (Becker & Aschenbach 2002; Pavlov et al. 2002; Pavlov et al. 2004)[2].

In addition, the absorbing column $N_H \sim 0.5 \times 10^{22}$ cm^{-2} of the diffuse emission around central source 1WGA J1713.4–3949 (top panel of Fig. 4 and Table 7) is consistent with the $0.47 \pm 0.03 \times 10^{22}$ cm^{-2} found for the two-component blackbody model (Table 6). Note that this is also

---

[2] The resemblance of RX J1713.7–3946 to "Vela Junior" is particularly striking since both remnants have an identical type of central point source at the center (no optical nor radio counterparts, absence of pulsations, same temperature, luminosity and surface emitting radius), are X-ray synchrotron dominated, have a weak and quite complex radio emission, are found in a complex environment and present an extremely low density of thermally emitting material (Slane et al. 2001).

Table 3. Best fit parameters for the power-law plus equilibrium model using the MOS and pn data all at once. The errors are in the range $\Delta\chi^2 < 2.7$ (90% confidence level) on one parameter. The regions are shown in Fig. 8. *Norm* is given in units of photons/cm^2/s/keV/arcmin^2 at 1 keV.

Region	χ^2 (d.o.f.)	N_H (10^{22} cm^{-2})	Γ	*Norm*	kT_e (keV)	$\int n_e n_H$ dl (cm^{-5})
1	933 (907)	0.77 (0.74–0.80)	2.45 (2.39–2.52)	7.00e−5 (6.51–7.31)	0.48 (0.36–0.60)	8.75e15 (5.76–12.30)
2	504 (466)	0.70 (0.66–0.75)	2.83 (2.75–2.94)	8.43e−5 (8.07–9.49)	0.61 (0.58–0.66)	2.55e16 (1.77–3.48)
3	499 (493)	0.57 (0.53–0.60)	2.59 (2.51–2.70)	3.73e−5 (3.49–4.22)	0.76 (0.70–0.83)	1.72e16 (1.25–2.33)
4	532 (516)	0.92 (0.87–0.96)	2.34 (2.27–2.42)	9.67e−5 (8.59–9.97)	0.79 (0.62–1.01)	1.27e16 (0.53–2.00)
5	646 (630)	0.75 (0.73–0.77)	2.52 (2.47–2.56)	1.80e−4 (1.74–1.99)	0.54 (0.42–0.66)	1.45e16 (0.76–2.64)
6	717 (640)	0.89 (0.85–0.92)	2.40 (2.35–2.45)	2.59e−4 (2.45–2.77)	0.61 (0.47–0.69)	2.45e16 (1.56–3.48)
7	383 (354)	0.95 (0.89–1.02)	2.20 (2.12–2.27)	1.64e−4 (1.50–1.80)	0.28 ($\leq$0.45)	1.08e16 (0.55–1.65)
8	807 (759)	1.13 (1.09–1.18)	2.58 (2.53–2.63)	3.32e−4 (3.12–3.54)	0.61 (0.43–0.73)	1.29e16 (0.66–1.82)
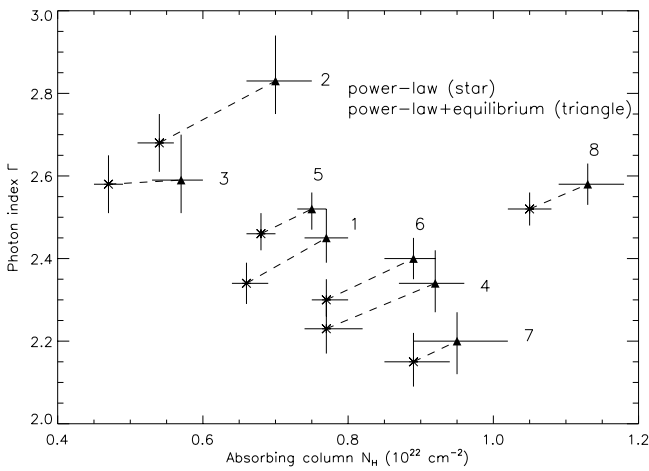
Fig. 9. For each of the 8 regions considered (see Fig. 8), changes of the parameters (N_H, Γ) with the addition of a thermal component. The star correspond to the power-law model (cf. Table 2). The black triangle correspond to the power-law plus thermal equilibrium model (cf. Table 3). The error bars are given at a 90% confidence level.

Table 4. Values of postshock electronic number density for a few regions (see Fig. 8) using Eq. (1) with $\theta_s = 32'$. D_1 is the distance in units of 1 kpc. The selected regions are those for which the thermal emission is detected for temperatures of $\sim$0.5−0.6 keV.

Region	θ_r (′)	$\hat{n}_e$ ($10^{-2} D_1^{-1/2}$ cm^{-3})
1	28	1.95 (1.58–2.31)
2	9	2.37 (1.97–2.76)
6	14	2.40 (1.91–2.86)
8	20	1.87 (1.33–2.22)

true considering the bremsstrahlung model which leads to a still acceptable $N_H \sim 0.7 \times 10^{22}$ cm^{-2} (Table 5) but is weakened adopting the blackbody+power-law model which yields a too high (almost a factor 2) column density $N_H \sim 0.9 \times 10^{22}$ cm^{-2} (Table 6).

Thus, it is highly probable that the point source 1WGA J1713.4–3949 is the compact relic of the supernova progenitor ranking RX J1713.7–3946 in the category of type II supernovae with strong particle acceleration.

4.2. Interaction with clouds and distance estimate

The mapping of the CO emission at 8′ resolution shown in SL99 has revealed the presence of three dense and massive clouds probably belonging to the same molecular complex of a Galactic arm at 6 kpc. An enhanced intensity ratio of the two lowest rotational transition of the CO molecule was found in one of these clouds located north of RX J1713.7–3946 suggesting that the SNR shock front is hitting this cloud. Based on this interaction, it was concluded that the remnant should be at a distance of 6 kpc.

On the other hand, *XMM-Newton* has revealed a positive correlation between the absorbing column density and the synchrotron X-ray brightness (see Fig. 6), which strongly suggests that the brightest regions of the SNR interact with part of the line-of-sight absorbing material (cf. Sect. 3.2). In particular, this is the case of the bright southwestern region which exhibits the strongest absorption in the line-of-sight. At 6 kpc, however, the three dense and massive CO clouds are observed in the north of the remnant; none is observed in the SW (SL99) where the highest absorption and a clear interaction are found with *XMM-Newton*.

Independent information on the absorption in the line-of-sight of SNR RX J1713.7-3946 can be obtained from a map of integrated optical star light. The optical star light is sensitive to the whole line-of-sight, but it should reflect column density variations. Figure 11 shows the *red DSS* optical image. The absorption morphology in the optical is quite different from the 6 kpc CO emission morphology presented in SL99 but similar to the X-ray absorption map. The optical brightness appears to be high in the X-ray faint CE and seems particularly weak in the X-ray bright SW region. If we extract the optical brightness and N_H for each pixel of the mapping grid (Sect. 2.3.4), we obtain a one dimensional plot of these two quantities. Figure 12 shows the very good inverse correlation obtained between our inferred column density and the optical brightness towards RX J1713.7-3946. This is consistent with the low and high absorptions found in the N_H map in the CE and SW, respectively (Fig. 4, left panel). This last result provides additional support for the reliability of the N_H distribution derived from the X-ray measurements.
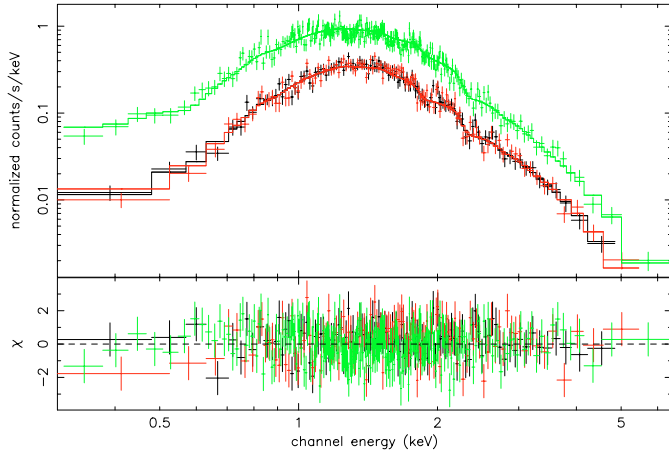
Fig. 10. EPIC spectra of the central source 1WGA J1713.4–3949 of the SNR RX J1713.7–3946 (MOS1 in black, MOS2 in red and pn in green). Best-fit obtained with a double blackbody model.

The disagreement between the absorption morphology towards RX J1713.7-3946 and the molecular gas distribution at 6 kpc has an immediate consequence either for the distance of the SNR or for the nature of the material interacting with the SNR. If RX J1713.7-3946 is really located at 6 kpc, this implies that the remnant interacts with an interstellar component of a different nature than molecular gas, such as HI gas for instance. In the other alternative, if RX J1713.7-3946 is really impacting molecular clouds, this implies that RX J1713.7-3946 is situated at a distance less or larger than 6 kpc. Because there is no evidence that the absorption toward the SNR is strongest in the north, contrary to what is observed in the CO map integrated up to 6 kpc (Bronfman et al. 1989, SL99), it indicates that the remnant must be located at a distance less than 6 kpc.

An indirect estimate of the density of the absorbing material located in the SW can be obtained from the local variations of column density in the interacting regions. We assume that the angular size θ_{abs} of the absorbing material is the same along the line-of-sight and in projection on the sky. If it is so, the density of the absorbing matter n_{abs} is given by:

$$n_{abs} = 1.11 \times 10^4 \left(\frac{D}{1\,\text{kpc}}\right)^{-1} \left(\frac{\theta_{abs}}{1'}\right)^{-1} \left(\frac{\Delta N_H}{10^{22}\,\text{cm}^{-2}}\right) \text{cm}^{-3} \quad (2)$$

where D is the SNR distance and ΔN_H is the variation of the absorbing column density between two regions separated by an angular size θ_{abs}. Typically in the SW (see left panel of Fig. 4), $\theta_{abs} \sim 15'$ and $\Delta N_H \simeq 0.4 \times 10^{22}$ cm^{-2}. This gives $n_{abs} \simeq 300 \left(\frac{D}{1\,\text{kpc}}\right)^{-1}$ cm^{-3} which corresponds to 50 cm^{-3} for a distance of the SNR of 6 kpc or 300 cm^{-3} for 1 kpc, a typical value for cold interstellar molecular clouds (e.g. Tatematsu et al. 1990; Wilner et al. 1998).

The pending question is then to determine the nature and the distance of the matter interacting with RX J1713.7–3946. Since the strongly absorbed regions are mainly found at the limit or around the SNR (particularly in the NW and SW) and not inside, a possible scenario would be that the remnant is within a wind-blown bubble created by the precursor star, and that the SN shock is encountering the wall of such a bubble, as

previously suggested (SL99, Ellison et al. 2001). However, the optical image shows that the thickness of the regions of lowest optical brightness found at the edges of the remnant (Fig. 11) is much higher than that expected from a stellar wind shell. Then, the most plausible picture is that of preexisting interstellar clouds, possibly pushed by the progenitor stellar wind, being struck by the SNR shock front. This can be tested by CO and HI observations.

We have reanalyzed the behaviour of the absorbing material across the SNR RX J1713.7-3946 based on data from the CfA CO survey (Dame et al. 2001) and from the IAR High Sensitivity HI survey (Arnal et al. 2000). The angular resolution of the CO J:1–0 data is $8.8'$, the grid sampling of $7.5'$ and the velocity resolution of 1.3 km s^{-1} (note that although Dame et al.'s 2001 new survey improves the sampling interval to half a beamwidth, the region containing the SNR RX J1713.7-3946 in the fourth Galactic quadrant is still based on the coarser sampling as published by Bronfman et al. 1989). For the HI data the angular resolution and the sampling are $30'$ and the velocity resolution is 1.03 km s^{-1}.

Figure 13 (top panel) displays the cumulative absorbing column density $N_H = N(HI) + 2 \times N(H_2)$ as a function of the *Local Standard of Rest* (LSR) radial velocity, towards the NW (continuous line), the SW (dotted line) and the center (dashed line). The plotted curves to the NW and SW were obtained from the average over ~8$'$ areas centered near $\alpha_{J2000} = $ 17h11m45s, $\delta_{J2000} = -39°32'45''$ and near $\alpha_{J2000} = $ 17h11m50s, $\delta_{J2000} = -39°57'00''$, respectively. The third N_H curve was calculated for a line-of-sight directed to the bright central X-ray point-like source 1WGA J1713.4–3949. The H_2 column density was calculated from the carbon monoxide distribution by adopting the molecular mass calibration ratio $X = (1.8 \pm 0.3) \times 10^{20}$ cm^{-2} (Dame et al. 2001). The behaviour of Fig. 13 (top panel) is mainly defined by the CO profile because of the better angular resolution of these data as compared with the HI survey used and its dominant contribution. The galactic rotation curve for $l = 347.5°, b = -0.5°$ (from Fich et al.'s 1989 circular galactic rotation model) is plotted in Figure 13 (bottom panel) for comparison. Table 7 gives the value of the cumulative absorbing column density towards the NW, SW and center for several LSR radial velocities or equivalently for several distances (only the closer distance is provided).

The line-of-sight towards $l = 347.5°$ basically crosses three galactic arms: Sagittarius, at an approximate distance of 1.4 kpc ($V_{LSR} \sim -10$ km s^{-1}), Scutum–Crux at about 3.7 kpc ($V_{LSR} \sim -34$ km s^{-1}), and Norma at about 5.3 kpc ($V_{LSR} \sim -66$ km s^{-1}) (Georgelin & Georgelin 1976). Figure 14 displays two average spectra obtained towards the NW (continuous line) and towards the SW (dotted line), where, in addition to the local gas, the three important galactic components are evident.

From the X-ray absorption map (see Fig. 4, left panel), the absorbing column density was found to be higher in the SW ($N_H \sim 0.8-1.1 \times 10^{22}$ cm^{-2}) than in the NW ($N_H \sim 0.6-0.7 \times 10^{22}$ cm^{-2}). The N_H curve obtained to the SW from CO and HI observations, lies above the curve obtained for the NW region only for velocities below $V_{LSR} \sim -23$ km s^{-1} as shown in Fig. 13 (top panel). Although the limited angular resolution

Table 5. Best fit parameters for different one component spectral models for 1WGA J1713.4–3949 using the MOS and pn data all at once. The errors are in the range $\Delta\chi^2 < 2.7$ (90% confidence level) on one parameter. D_1 is the distance in units of 1 kpc.

One component model	kT (keV)	R (D_1 km)	L ($10^{33}\ D_1^2$ erg s^{-1})	Γ	N_H (10^{22} cm^{-2})
Power law				4.24	1.10
$\chi^2 = 740$ (475 d.o.f.)				(4.18–4.30)	(1.07–1.13)
Blackbody	0.41	0.37	0.49		0.35
$\chi^2 = 622$ (475 d.o.f.)	(0.40–0.42)	(0.36–0.38)	(0.47–0.51)		(0.33–0.37)
Bremsstrahlung	0.94				0.70
$\chi^2 = 499$ (475 d.o.f.)	(0.92–0.96)				(0.68-0.72)

Table 6. Best fit parameters for different two components spectral models for 1WGA J1713.4–3949 using the MOS and pn data all at once. The errors are in the range $\Delta\chi^2 < 2.7$ (90% confidence level) on one parameter. D_1 is the distance in units of 1 kpc.

Two components model	kT (keV)	R (D_1 km)	$L\ 10^{33}$ (D_1^2 erg s^{-1})	Γ	N_H (10^{22} cm^{-2})
Blackbody	0.40	0.31	0.32		0.91
+	(0.38–0.42)	(0.28–0.36)	(0.28–0.35)		(0.85–0.97)
Power law				4.25	
$\chi^2 = 503$ (473 d.o.f.)				(4.03–4.50)	
Blackbody	$kT_1 = 0.57$	$R_1 = 0.59$	$L_1 = 0.17$		0.47
+	(0.52–0.64)	(0.51–0.69)	(0.14–0.23)		(0.44–0.51)
Blackbody	$kT_2 = 0.32$	$R_2 = 0.11$	$L_2 = 0.44$		
$\chi^2 = 490$ (473 d.o.f.)	(0.29–0.34)	(0.07–0.16)	(0.40–0.48)		

Table 7. Values of the accumulative absorbing column density towards the NW, SW and CE as obtained from CO and HI observations for several LSR radial velocities or equivalently for several distances. The values of N_H which are in bold font are those compatible with the X-rays.

V_{LSR}	D	N_H (10^{22} cm^{-2})		
(km s^{-1})	(kpc)	NW	SW	CE
–0.4	0.14	0.43	0.50	0.38
–3.0	0.58	0.52	0.60	0.48
–5.6	**0.98**	**0.62**	**0.71**	**0.56**
–8.2	**1.33**	**0.74**	**0.83**	**0.65**
–10.9	**1.67**	**0.89**	**0.97**	**0.76**
–13.5	1.97	1.03	1.12	0.85
–16.0	2.24	1.14	1.22	0.92
–18.6	2.50	1.21	1.28	0.97
–21.2	2.74	1.27	1.33	1.01
–23.8	2.96	1.35	1.37	1.05
–26.5	3.17	1.44	1.42	1.08

of the available HI data "dilutes" small spatial variations and reduces the ΔN_H between the two regions, this sets an upper limit on the SNR distance at ~2.9 kpc using the galactic rotation curve (Fig. 13, bottom panel).

The absorbing column densities derived from the *XMM-Newton* data are found to be $0.4-0.6 \times 10^{22}$ cm^{-2} towards 1WGA J1713.4–3949, $0.6-0.7 \times 10^{22}$ cm^{-2} towards the NW, and $0.8-1.1 \times 10^{22}$ cm^{-2} towards the SW (Sect. 3.2). These values match very well those found from the CO and HI observations if the LSR radial velocity range is between ~−6

and ~−11 km s^{-1} as indicated on Table 7. Then, it reduces the SNR distance range to ~0.9−1.7 kpc.

The only negative LSR velocities for which the CO emission is clearly higher in the SW than in NW are found between 0 and −10 km s^{-1} as revealed by the spectra displayed in Fig. 14. Indeed, the presence of a "shoulder" of higher emission obtained to the SW (dotted line) can be noticed, as compared to the NW spectra (solid line). This constitutes an evidence for the presence of molecular gas in the SW direction. This feature is consistent with the molecular cloud recently detected by Fukui et al. (2003) in the SW (between −3 and −11 km s^{-1}) on the basis of 2.6 mm CO J:1–0 observations carried out with the *NANTEN* telescope. The range of LSR velocities corresponding to the upper limit distance of 1.6 kpc, using the circular galactic rotation model (Fich et al. 1989), is compatible with the allowed distance range of ~0.9−1.7 kpc.
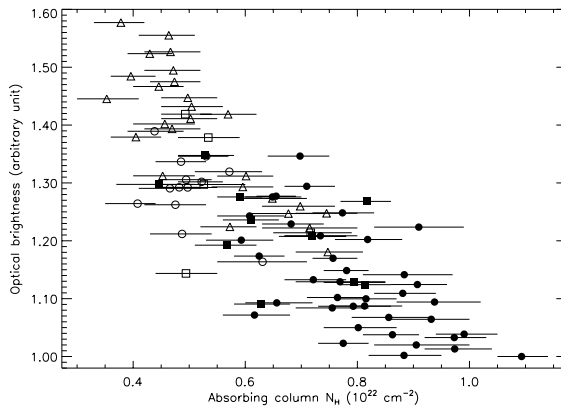
A search for the ground-state satellite line of the hydroxyl molecule at 1720.53 MHz was carried out towards two spots in G347.3-0.5 where both X-rays and CO observations suggested strong shock/molecular cloud interaction. The positive detection of OH (1720 MHz) masers permits us to confirm the existence of such interaction and to constrain the physical parameters of the shock-excited gas on the basis of the very specific conditions required to excite the 1720 MHz OH masers.

The observations were carried out with the Very Large Array of NRAO[3] in the C-configuration for 2 h on March 11, 2004. Two 22′ fields centered at (17h11m45s, −39°57′30″) and (17h11m45s, −39°57′30″) were observed. A 256-channel
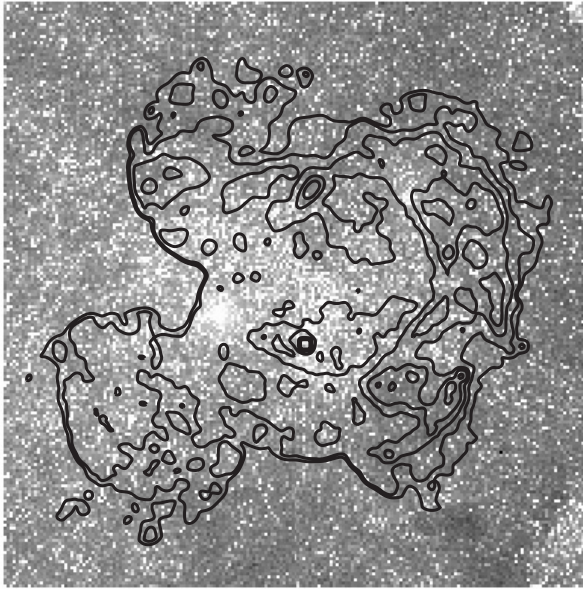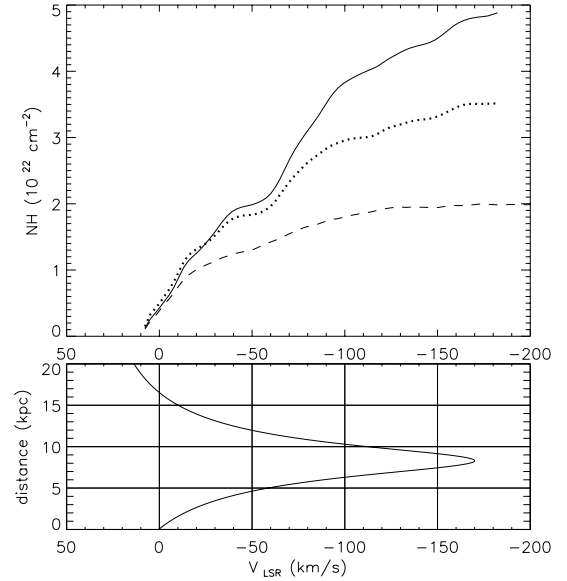
Fig. 11. Optical image between 2300 and 3000 Å (*Second Generation Digitized Sky Survey* in red color at 450–600 THz) overlaid with the contour of the 2–10 keV X-ray image of SNR RX J1713.7–3946. The scaling is linear with the higher cut fixed at 5σ of the mean optical brightness value.
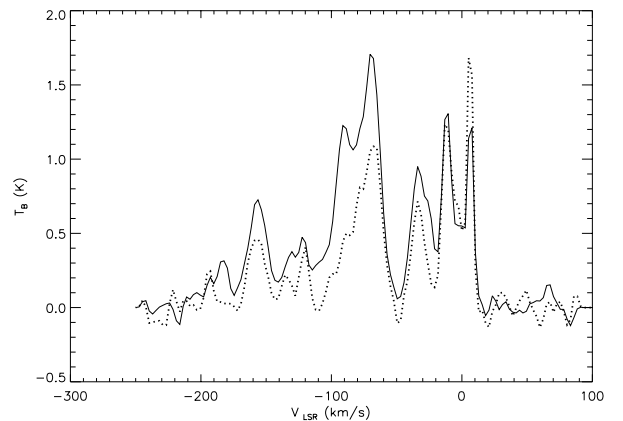

Fig. 13. *Top panel*: the cumulative absorbing column density as obtained from the atomic and molecular hydrogen, as a function of radial velocity. The continuous line corresponds to the average NH estimated towards the NW region, the dotted line corresponds to the SW region and the dashed line to a line-of-sight directed to 1WGA J1713.4-3949. *Bottom panel*: the rotation curve towards $l = 347.5$, $b = -0.5$ as obtained from Fich et al.'s (1989) circular galactic rotation model.

Fig. 12. Correlation plot between the absorbing column N_H (in units of 10^{22} cm^{-2}) and the normalized optical brightness. To obtain this plot, the optical image shown in Fig. 11 has been cut following the absorbing column map grid. Each point corresponds to the value found for a particular pixel of the mapping grid (Sect. 2.3.4) and the error bars are given at a 90% confidence level. The symbols are defined as in Table 1.

Fig. 14. Average CO spectra obtained towards the NW (continuous line) and towards the SW (dotted line) from the CfA CO survey (Dame et al. 2001). The SW emission is higher than the NW emission for LSR velocities between 0 and -10 km s^{-1}.

spectrometer centered around -30 km s^{-1}, with a channel width of 3.05 kHz/channel (~ 0.5 km s^{-1} at 1720 MHz) and a velocity range $\Delta v \sim 134$ km s^{-1}, was used. The data were cleaned and calibrated using AIPS routine programs. The synthesized beam was $40'' \times 10''$ and the noise level of about 50 μJy/beam per channel.

The results of the search for OH (1720 MHz) masers were negative. This fact is probably due either to the fact that the shocked molecular clouds have a volume density smaller than that required to excite the masers, or the shock front was not of a non-dissociative C-type (Wardle 1999).

The X-ray analysis of SNR RX J1713.7–3946 with *XMM-Newton* has revealed a strong absorption in the SW, even stronger than in the NW. The absorption derived from the optical star brightness is in agreement with the X-ray derived map. This high absorption found in the SW was unexpected with regard to the morphology of the CO distribution at 6 kpc. Moreover, the positive correlation between X-ray absorption and the X-ray brightness indicates that the shock front of RX J1713.7–3946 is impacting the molecular clouds responsible for the absorption. The CO and H I observations show that the inferred cumulative absorbing column densities are in excellent agreement with the X-ray findings in different places of the remnant provided that the SNR lies at a distance of

1.3 ± 0.4 kpc, probably in the Sagittarius galactic arm. Other indications of an interaction between the SNR blast-wave and molecular clouds are provided by the existence of an excess of fast-moving HI gas (Koo et al. 2004) and possibly, the existence of a broad CO profile in LSR velocity found in a coincident bright X-ray feature in the SW at 1 kpc (Fukui et al. 2003). Based on the absorption morphology and the probable association between the SNR and the molecular clouds, the distance of SNR RX J1713.7–3946 is revised to 1.3 ± 0.4 kpc instead of the commonly accepted value of 6 kpc.

4.3. Particle acceleration

The asymmetry in the synchrotron X-ray emission morphology is the result of the asymmetry in the ambient density around the remnant. In the strongly absorbed bright SW rim, we have established that the shock front of RX J1713.7–3946 is interacting with molecular clouds as suggested by the positive correlation between X-ray absorption and X-ray brightness. In the weakly absorbed faint SE region, the same correlation suggests that the shock front of RX J1713.7–3946 is propagating into a tenuous ambient medium which is consistent with the larger extent of the SNR there than in the SW. In Sect. 3.2, we looked at the spatial modifications (in the SW and SE) of particle acceleration at the shock in RX J1713.7–3946 through the photon spectral index changes. The regions where the shock impacts the molecular clouds have a steeper spectrum ($\Gamma \sim 2.3$–2.7) than those where the shock propagates into a low density medium ($\Gamma \sim 1.9$–2.2).

Qualitatively, we can interpret such modifications in the synchrotron spectrum by considering a modification of the acceleration in the interaction region with dense molecular clouds. To investigate this, we used a simple model of non-linear diffusive shock acceleration (Berezhko & Ellison 1999; Ellison et al. 2000) varying the upstream density n_0, the shock speed V_{sk} and the magnetic field B_0 for an injection (i.e. fraction of gas particles which are accelerated) set to 10^{-3}. As the SNR blast-wave runs into a high density medium such as molecular clouds, its velocity is expected to diminish according to the ram pressure conservation ($n_0 V_{sk}^2$ constant) and the upstream magnetic field is expected to increase following the square root of the density ($B_0 n_0^{-1/2}$ constant). The result of the density increase is to lead to a steepening of the synchrotron spectrum but no increase in brightness. Therefore, this cannot explain the observed difference in X-ray brightness between the SE and the SW (for the same magnetic field orientation). However, if the shock is preferentially tangential in the region of high density but normal in the region of lower density, the X-ray brightness can be strongly enhanced due to the compression of the downstream magnetic field on condition that the density contrast between the two regions is weak (not more than a factor 4). Then, it is possible to explain stronger X-ray brightness and a steeper synchrotron spectrum in the SW than in the SE if the magnetic field is tangential in the SW but normal in the SE and if the acceleration process occured before the shock entered the dense molecular clouds.

A modeling of these effects is beyond the scope of this paper. Further smaller scale spectral studies with the *Chandra* satellite would help to investigate the origin of the steepening of the spectrum in the SW.

4.4. SNR age and energetics

The study of the thermal emission with *XMM-Newton* has lead to an upper limit on the density in the ambient medium of $n_0 \leq 2 \times 10^{-2} D_1^{-1/2}$ cm^{-3} where D_1 is the distance in units of 1 kpc (cf. Sect. 3.3). If the density derived from the emission measure is indeed representative of the density in the ambient medium (which is not the case in the radiative phase), an estimate of the swept-up mass is given by:

$$M_{sw} \sim 2.96 \times 10^{-3} \left(\frac{D}{1 \text{ kpc}}\right)^3 \left(\frac{\theta_s}{1'}\right)^3 \left(\frac{n_0}{1 \text{ cm}^{-3}}\right) M_\odot \qquad (3)$$

where θ_s is the angular size of the blast-wave radius. This leads to an upper limit on the swept-up mass of 1 $M_\odot$ for a distance of 1 kpc and $\theta_s = 32'$. If RX J1713.7–3946 is the remnant of a type II explosion, the initial mass of the progenitor is expected to be above 5–8 $M_\odot$ (Kennicutt 1984) and then the mass of the ejected matter of a few solar masses. This is well above the derived swept-up mass leading to the conclusion that RX J1713.7–3946 must be in the free expansion phase.

The hypothesis proposed by Wang et al. (1997), based on historical records, that RX J1713.7–3946 is the remnant of the supernova that exploded in AD 393 would imply an age of $t_s = 1600$ years. Assuming self-similar solutions (Chevalier 1982), we can estimate the shock velocity given by $v_s = 2.85 \times 10^2 (n-3)/(n-s) (D/1 \text{ kpc}) (\theta_s/1') (t_s/10^3 \text{ yr})^{-1}$ km s^{-1} where n and s are the power-law indexes of the initial outer density profile in the ejecta and of the initial ambient medium density profile, respectively. $n \sim 9$–12 is typical of SN II, $s = 0$ corresponds to an homogeneous ambient medium, $s = 2$ to an ambient medium modified by the progenitor wind. For $n = 9$, $v_s \simeq 3.8 \times 10^3$ km s^{-1} if $s = 0$ and $v_s \simeq 4.9 \times 10^3$ km s^{-1} if $s = 2$.

The determination of the kinetic energy of the explosion provides a strong argument for or against the hypothesis that RX J1713.7–3946 is the remnant of the AD 393 stellar explosion. In the framework of a spherical self-similar model (Chevalier 1982), we can estimate the kinetic energy of the explosion as a function of the SNR age for different progenitor masses and ambient medium densities. The energy curves depend on three parameters among which n and s for a given progenitor mass (Decourchelle & Ballet 1994). The power-law index n of the ejecta density profile was fixed to 9. The power-law index s of the ambient density profile was fixed to 0 to simulate a flat ambient medium which seems to be the situation in the SE. The kinetic energy of the explosion is then determined by the relation:

$$E_{SN} = \frac{3}{10}(n-5)^{-1}(n-3)^{(n-5)/(n-3)} \left(\frac{4\pi n \rho_0}{3A}\right)^{2/(n-3)}$$
$$\times (\epsilon r_s)^{2(n-s)/(n-3)} M_{ej}^{(n-5)/(n-3)} t_s^{-2} \qquad (4)$$
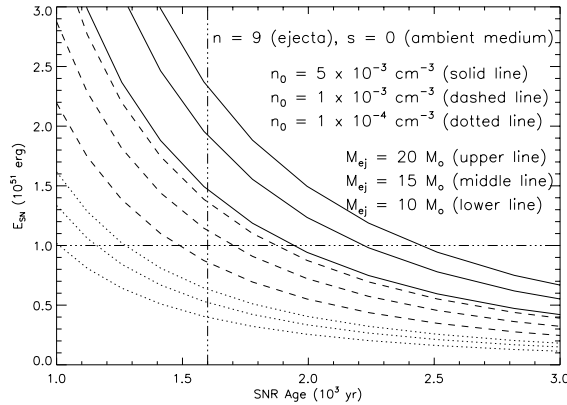
Fig. 15. Kinetic energy of the explosion as a function of the SNR age for several solar masses of the supernova ejecta (M_{ej} = 10, 15 and 20 $M_\odot$) and different ambient medium densities (n_0 = 5×10^{-3}, 1×10^{-3} and 5×10^{-4} cm^{-3}).

where r_s is the shock radius set to 10 pc, $\rho_0 = 1.4\,m_H\,n_0$ and t_s the SNR age. The parameters A and ϵ are determined by solving the self-similar hydrodynamical equations (Chevalier 1982).

Energy curves are illustrated in Fig. 15 for supernova ejecta masses of M_{ej} = 10, 15 and 20 $M_\odot$ representative of type II supernova and for different ambient medium densities between 1×10^{-4} and 5×10^{-3} cm^{-3}. If we adopt the standard 10^{51} erg as the energy of the explosion, it shows that an ambient medium density of 10^{-3} cm^{-3} is appropriate for ejecta masses between 10 $M_\odot$ and 15 $M_\odot$ if we consider a remnant that is 1600 years old. At this age, the higher density of the ambient medium (5×10^{-3} cm^{-3}) leads to a higher kinetic energy of the explosion, which is still possible, whereas below 10^{-4} cm^{-3}, the kinetic explosion energy begins to be too weak

If we consider the effect of efficient cosmic-ray acceleration on the structure of the blast-wave as described in Chevalier (1983), energy curves move slightly higher and would only very slightly widen the range of allowed ambient medium densities. Hence, these results based on an energy argumentation are consistent with the picture of a young SNR expanding in a low density medium.

4.5. Evolutionary stage

Although the star formation process is complex, there is observational evidence that massive stars are born in the densest parts of molecular clouds. The presence of molecular clouds around the northern and southwestern parts of RX J1713.7–3946 strongly suggests that its progenitor star is indeed born in such conditions. Evolved SNRs interacting with molecular clouds are expected to be efficient electron accelerators (Bykov et al. 1999) as observed in RX J1713.7–3946. Nevertheless, these molecular clouds appear to be located at the periphery of the SNR at ~7 pc away from the center, assuming a distance of 1 kpc. Massive stars are known to initiate and maintain powerful stellar winds during their lives so that they can move the molecular clouds from the vicinity of the progenitor star. These winds may have homogenized the immediate environment of the progenitor star, explaining the

Table 8. Parameters for main sequence evolution for different progenitor masses $M_\star$ (from Chevalier 1999 and references therein). $\dot{M}_{loss}$ is the mass loss rate, L_w is the mechanical wind luminosity, t_{ms} is the main-sequence age and r_b is the maximum size of the wind bubble.

$M_\star$	Spectral	$\dot{M}_{loss}$	L_w	t_{ms}	r_b
($M_\odot$)	type	($M_\odot$ yr^{-1})	(erg s^{-1})	(yr)	(pc)
12	B1 V	6×10^{-9}	9.3×10^{32}	1.3×10^7	5.3
16	B0 V	6×10^{-8}	9.3×10^{33}	0.9×10^7	10.0

extremely low mean density inside the SNR (McKee et al. 1984; Chevalier 1999).

In the standard picture of a stellar wind interacting with the interstellar medium, a four-zone structure (Castor et al. 1975; Weaver et al. 1977) settles very rapidly, consisting of the innermost hypersonic stellar wind characterized by a density profile $\rho \propto r^{-2}$, a hot shocked stellar wind region, a shell of shocked interstellar medium and the ambient interstellar gas. After a few thousand years, the swept-up shocked interstellar gas collapses into a thin cold ($T \sim 10^4$ K) shell strongly affected by radiative losses while the low-density (<1 cm^{-3}) shocked stellar wind region occupying most of the bubble volume remains very hot ($T > 10^6$ K).

A possible interpretation of our observation of RX J1713.7–3946 is that the SN event occured in a wind-blown bubble. In the SE, the shock front of the remnant is still propagating into the low-density hot shocked wind ($n_0 \leq 0.02$ cm^{-3}). In the SW, the blast-wave of RX J1713.7–3946 has already progagated into the shocked stellar wind and is impacting the cold and dense (~300 cm^{-3}, see Eq. (2)) shell of shocked ambient material. The remnant could be in the free expansion phase in the SE whereas in the radiative phase in the SW.

In this scenario, the size of the bubble provides an estimate of the strength of the wind and hence of the progenitor mass. From Fig. 2, the position of the bright X-ray rims in the NW and SW ($r_b \sim 6-9$ pc, taking into account the projection effects) provides an estimate of the radius of the bubble r_b, assuming that the molecular clouds have been removed from the vicinity of the star by the progenitor stellar wind.

Then, an estimate of the mass of RX J1713.7–3946's progenitor star can be obtained by directly comparing its wind-bubble size where the molecular clouds are located with those estimated from observations of stars of different masses. Table 8 shows two cases for which the bubble radii (5.3 and 10.0 pc) are close to the 6–9 pc values estimated in the NW and SW for RX J1713.7–3946. This implies that the mass of RX J1713.7–3946's progenitor must be between 12 and 16 $M_\odot$ in the main sequence evolution phase, which corresponds to a B-star whose lifetime on the main sequence is about 10^7 years. In Table 8, the mechanical wind luminosity $L_w \equiv \dot{M}_{loss} v_w^2 / 2$ is computed assuming an appropriate wind velocity $v_w = 700$ km s^{-1} as chosen in Chevalier (1999). The maximum size of the wind bubble is given by (in pc):

$$r_b = 10.7 \left(\frac{L_w}{10^{34}\,\text{erg s}^{-1}} \right)^{1/3} \left(\frac{p/k}{10^5\,\text{K cm}^{-3}} \right)^{-1/3} \left(\frac{t_{ms}}{10^7\,\text{yr}} \right)^{1/3} \quad (5)$$

assuming that the surrounding interclump medium exerts a pressure $p/k = 10^5$ K cm^{-3}, typical of cloud (Chevalier 1999).

From the characteristics of B-stars, we can estimate the mean density in the wind before the supernova event and compare it to the density derived from the thermal X-rays (see Sect. 3.3). The mass lost during the lifetime of the progenitor diluted in the volume of the bubble gives an estimate of the mean number density n_b of the wind-bubble (in cm^{-3}):

$$n_b = 6.9 \times 10^{-4} \left(\frac{\dot{M}_{loss}}{10^{-8} \, M_\odot \, yr^{-1}} \right) \left(\frac{t_{ms}}{10^7 \, yr} \right) \left(\frac{r_b}{10 \, pc} \right)^{-3}. \tag{6}$$

For $M_\star = 12$ and 16 $M_\odot$ (cf. Table 8), we obtain a mean density of 3.6×10^{-3} and 3.7×10^{-3} cm^{-3}, respectively. This is consistent with the $\sim 2 \times 10^{-2}$ cm^{-3} upper limit found for the thermal emission in the X-rays. Note that the mass lost in the red giant phase was not taken into account because it produces a local excess in density only in the vicinity of the progenitor star.

The proposed scenario in which the SNR blast wave expands into a low-density shocked wind medium in the SE and strikes molecular clouds in the SW appears to be a possible physical picture since the density derived from the thermal X-ray emission measures can be found to be consistent with the expected density in the pre-SN shocked stellar wind. However, it is hard to understand why the shell of molecular clouds shocked by the SNR blast-wave does not produce copious thermal X-ray emission since the X-ray brightness is proportional to the square of the density. The regions of enhanced X-ray emission as observed in the SW are those where there is a strong increase of the synchrotron X-ray emission (correlated with an increased of absorbing column density), but where there is no indication of any increase of the thermal X-ray emission.

However, if the SW rim of RX J1713.7–3946 is in the radiative phase, then we do not expect thermal X-ray emission from the shocked interstellar clouds. It would also explain why the thermal X-ray density does not follow the variations of the ambient density. A high density of 300 cm^{-3} and a temperature of 10^5 K in the shocked interstellar clouds yield a cooling time of ~ 25 years.

However, in SNRs where the shock is radiative, as observed in the Cygnus Loop, bright optical filaments are generally observed (Levenson et al. 1996). The optical emission is attributed to the cooling of the gas behind the shock front. This cooling gas emits many optical lines including hydrogen Balmer lines with a temperature of $\sim 10^4$ K. If RX J1713.7–3946 is indeed in the radiative phase where the blast wave has reached the cavity wall and is interacting with dense matter, such optical filaments might be visible, although the absorption along the line-of-sight is much stronger in RX J1713.7–3946 ($N_H \sim 10^{22}$ cm^{-2}) than in the Cygnus Loop SNR ($N_H \sim 4 \times 10^{20}$ cm^{-2}).

Finally, we could expect an enhancement of the thermal X-ray emission in the shocked stellar wind just behind the shocked shell. Indeed, a blast wave impacting on a dense cloud gives rise to both a reflected shock propagating back and a transmitted shock propagating into the cloud

(McKee & Cowie 1975). The shocks that are reflected off molecular cloud surfaces are expected to propagate back into the hot, previously shocked gas, further heating and compressing it (e.g. Levenson et al. 1996). Then, enhanced X-ray thermal emission is expected (Hester & Cox 1986). However, the density in the shocked gas is still small so that its contribution might be negligeable.

5. Conclusion

XMM-Newton observations have yielded several new results on SNR RX J1713.7–3946. The observation results and their astrophysical interpretation are summarized here:

– The X-ray bright central point source 1WGA J1713.4–3949 detected at the center of SNR RX J1713.7–3946 shows spectral properties very similar to those of the Compact Central Objects found in SNRs (e.g., Vela Junior) and which are consistent with the absorbing column density of the central diffuse X-ray emission arising from the SNR. It is highly probable that the point source 1WGA J1713.4–3949 is the compact relic of RX J1713.7–3946's supernova progenitor.

– The X-ray mapping of the absorbing column density has revealed strong variations (0.4×10^{22} cm^{-2} $\leq N_H \leq 1.1 \times 10^{22}$ cm^{-2}) and, particularly, an unexpected strong absorption in the southwest. The column density variations are well reflected by the extinction in the map of integrated optical star light. The strong positive correlation between the X-ray absorption and the X-ray brightness along the western rims suggests that the shock front of RX J1713.7–3946 is impacting molecular clouds there.

– CO and HI observations show that the inferred cumulative absorbing column densities are in excellent agreement with the X-ray measurements in different places of the remnant only if the SNR is placed at a distance of 1.3 ± 0.4 kpc, probably in the Sagittarius galactic arm, and not at 6 kpc as previously claimed. An excess in the CO emission found in the southwest at ~ 1 kpc strongly suggests that molecular clouds produce the enhancement in absorption. A search for OH masers in the southwestern region has been unsuccessful, possibly due to the low density of the clouds.

– The X-ray mapping of the photon index has revealed strong variations ($1.8 \leq \Gamma \leq 2.6$). The spectrum is steep in the faint central regions and flat at the presumed shock locations, particularly in the southeast. However, the regions where the shock strikes molecular clouds have a steeper spectrum than those where the shock propagates into a low density medium.

– The search for thermal emission from RX J1713.7–3946 remains unsuccessful leading to a number density upper limit of 2×10^{-2} cm^{-3} in the ambient medium. This low density in the ambient medium yields a reasonable kinetic energy of the explosion provided that the remnant is less than a few thousand years old. It can be reconciled with the high density in molecular clouds if the remnant is in the radiative phase where the SNR shock encounters a dense

ambient medium whereas it is in the free expansion phase elsewhere.

- RX J1713.7–3946's progenitor mass is estimated to lie between 12 and 16 $M_\odot$ based on a scenario involving the effect of stellar wind of the progenitor star.

References

Arnal, E. M., Bajaja, E., Larrarte, J. J., Morras, R., & Poppel, W. 2000, A&AS, 142, 35

Arnaud, M., Neumann, D. M., Aghanim, N., et al. 2001, A&A, 365, L80

Arnaud, M., Majerowicz, S., Lumb, D., et al. 2002, A&A, 390, 27

Arnaud, K. A. 1996, Astronomical Data Analysis Sofware and Systems V, ed. G. Jacoby, & J. Barnes, ASP Conf. Ser., 101, 17

Becker, W., & Aschenbach, B. 2002, Proceedings of the 270, WE-Heraeus Seminar on Neutrons Stars, Pulsars and Supernova Remnants

Berezhko, E. G., & Ellison, D. C. 1999, ApJ, 526, 385

Bronfman, L., Alvarez, H., Cohen, R. S., & Thaddeus, P. 1989, ApJS, 71, 481

Butt, Y. M., Torres, D. F., Combi, J. A., Dame, T., & Romero, G. E. 2001, ApJ, 562, L167

Butt, Y. M., Torres, D. F., Romero, G. E., Dame, T. M., & Combi, J. A. 2002, Nature, 418, 499

Bykov, A. M., Chevalier, R. A., Ellison, D. C., & Uvarov, Y. A. 2000, ApJ, 538, 203

Cassam-Chenaï, G., Decouchelle, A., Ballet, J., et al. 2004a, A&A, 414, 545

Cassam-Chenaï, G., Decouchelle, A., Ballet, J., & Dubner, G. 2004b, Young Neutron Stars and Their Environments, IAU Symp., 218, ed. F. Camilo, & B. M. Gaensler

Castor, J., McCray, R., & Weaver, R. 1975, ApJ, 200, L107

Chevalier, R. A. 1982, ApJ, 258, 790

Chevalier, R. A. 1983, ApJ, 272, 765

Chevalier, R. A. 1999, ApJ, 511, 798

Crawford, F., Pivovaroff, M. J., Kaspi, V. M., & Manchester, R. N. 2002, Neutrons Stars in Supernova Remnants, ASP Conf. Ser., 9999, ed. P. O. Slane, & B. M. Gaensler

Dame, T. M., Hatmann, D., & Thaddeus, P. 2001, ApJ, 547, 792

Decourchelle, A., & Ballet, J. 1994, A&A, 287, 206

Ellison, D. C., Berezhko, E. G., & Baring, M. G. 2000, ApJ, 540, 292

Ellison, D. C., Slane, P., & Gaensler, B. M. 2001, ApJ, 563, 191

Enomoto, R., Tanimori, T., Naito, T., et al. 2002, Nature, 416, 823

Fich, M., Blitz, L., & Stark, A. A. 1989, ApJ, 342, 272

Fukui, Y., Moriguchi, Y., Tamura, K., et al. 2003, PASJ, 55, L61

Georgelin, Y. M., & Georgelin, Y. P. 1976, A&A, 49, 57

Hartman, R. C., Bertsch, D. L., Bloom, S. D., et al. 1999, ApJS, 123, 79

Hester, J. J., & Cox, D. P. 1986, ApJ, 300, 675

Kargaltsev, O., Pavlov, G. G., Sanwal, D., & Garmire, G. P. 2002, ApJ, 580, 1060

Koyama, K., Petre, R., Gotthelf, E. V., et al. 1995, Nature, 378, 255

Koyama, K., Kinugasa, K., Matsuzaki, K., et al. 1997, PASJ, 49, L7

Kennicutt, R. C. 1984, ApJ, 277, 361

Koo, B.-C., Kang, J., & McClure-Griffiths, N. 2004, Young Neutron Stars and Their Environments, IAU Symp., 218, ed. F. Camilo, & B. M. Gaensler

Lazendic, J. S., Slane, P. O., Gaensler, B. M., et al. 2003, ApJ, 593, L27

Lazendic, J. S., Slane, P. O., Gaensler, B. M., et al. 2004, ApJ, 602, 271

Levenson, N. A., Graham, J. R., Hester, J. J., & Petre, R. 1996, ApJ, 468, 323

McKee, C. F., Van Buren, D., & Lazareff, B. 1984, ApJ, 278, L115

McKee, C. F., & Cowie, L. L. 1975, ApJ, 195, 715

Muraishi, H., Tanimori, T., Yanagita, et al. 2000, A&A, 354, L57

Pannuti, T. G., Allen, G. E., Houck, J. C., & Sturner, S. J. 2003, ApJ, 593, 377

Pavlov, G. G., Sanwal, D., Garmire, G. P., & Zavlin, V. E. 2002, Neutron Stars in Supernova Remnants, ed. P. O. Slane, & B. M. Gaensler, ASP Conf. Ser., 271, 247

Pavlov, G. G., Sanwal, D., & Teter, M. A. 2004, Young Neutron Stars and Their Environments, IAU Symp., 218, ed. F. Camilo, & B. M. Gaensler

Pfeffermann, E., & Aschenbach, B. 1996, in Roentgenstrahlung from the Universe, ed. H. H. Zimmermann, J. Trümper, & H. Yorke (MPE Rep. 263; Garching: MPE), 267

Read, A. M., & Ponman, T. J. 2003, A&A, 409, 395

Reimer, O., & Pohl, M. 2002, A&A, 390, L43

Reynolds, S. P. 1998, ApJ, 493, 375

Slane, P., Gaensler, B. M., Dame, T. M., et al. 1999, ApJ, 525, 357, SL99

Slane, P., Hughes, J. P., Edgar, R. J., et al. 2001, ApJ, 548, 814

Tatematsu, K., Fukui, Y., Iwata, T., Seward, F. D., & Nakano, M. 1990, ApJ, 351, 157

Tsurata, S. 1998, Phys. Rep., 292, 1

Uchiyama, Y., Aharonian, F. A., & Takahashi, T. 2003, A&A, 400, 567

Wang, Z.-R., Qu, Q.-Y., & Chen, Y. 1997, A&A, 318, L59

Wardle, M. 1999, ApJ, 525, L101

Weaver, R., McCray, R., & Castor, J. 1977, ApJ, 218, 377

Willingale, R., Aschenbach, B., Griffits, R. G., et al. 2001, A&A, 365, L212

Wilner, D. J., Reynolds, S. P., & Moffett, D. A. 1998, AJ, 115, 247